Astronomy & Astrophysics manuscript no. output
January 26, 2026

Euclid: Discovery of bright $z \simeq 7$ Lyman-break galaxies in UltraVISTA and *Euclid* COSMOS⋆

R. G. Varadaraj⋆⋆[1], R. A. A. Bowler[2], M. J. Jarvis[1,3], J. R. Weaver[4], E. Bañados[5], P. Holloway[1,6], K. I. Caputi[7,8], S. M. Wilkins[9], D. Yang[10], B. Milvang-Jensen[8,11], L. Gabarra[1], P. A. Oesch[12,8,11], A. Amara[13], S. Andreon[14], N. Auricchio[15], C. Baccigalupi[16,17,18,19], M. Baldi[20,15,21], S. Bardelli[15], A. Biviano[17,16], E. Branchini[22,23,14], M. Brescia[24,25], S. Camera[26,27,28], G. Cañas-Herrera[29,10], V. Capobianco[28], C. Carbone[30], J. Carretero[31,32], M. Castellano[33], G. Castignani[15], S. Cavuoti[25,34], K. C. Chambers[35], A. Cimatti[36], C. Colodro-Conde[37], G. Congedo[38], C. J. Conselice[2], L. Conversi[39,40], Y. Copin[41], F. Courbin[42,43,44], H. M. Courtois[45], M. Cropper[46], A. Da Silva[47,48], H. Degaudenzi[12], G. De Lucia[17], H. Dole[49], F. Dubath[12], C. A. J. Duncan[38], X. Dupac[40], S. Dusini[50], S. Escoffier[51], M. Farina[52], R. Farinelli[15], F. Faustini[33,53], S. Ferriol[41], F. Finelli[15,54], P. Fosalba[55,56], N. Fourmanoit[51], M. Frailis[17], E. Franceschi[15], M. Fumana[30], S. Galeotta[17], K. George[57], B. Gillis[38], C. Giocoli[15,21], J. Gracia-Carpio[58], A. Grazian[59], F. Grupp[58,60], L. Guzzo[61,14,62], S. V. H. Haugan[63], J. Hoar[40], H. Hoekstra[10], W. Holmes[64], I. M. Hook[65], F. Hormuth[66], A. Hornstrup[67,68], K. Jahnke[5], M. Jhabvala[69], B. Joachimi[70], E. Keihänen[71], S. Kermiche[51], A. Kiessling[64], M. Kilbinger[72], B. Kubik[41], M. Kümmel[60], M. Kunz[73], H. Kurki-Suonio[74,75], A. M. C. Le Brun[76], S. Ligori[28], P. B. Lilje[63], V. Lindholm[74,75], I. Lloro[77], G. Mainetti[78], D. Maino[61,30,62], E. Maiorano[15], O. Mansutti[17], O. Marggraf[79], M. Martinelli[33,80], N. Martinet[81], F. Marulli[82,15,21], R. J. Massey[83], E. Medinaceli[15], S. Mei[84,85], M. Melchior[86], Y. Mellier[87,88], M. Meneghetti[15,21], E. Merlin[33], G. Meylan[89], A. Mora[90], M. Moresco[82,15], L. Moscardini[82,15,21], R. Nakajima[79], C. Neissner[91,32], S.-M. Niemi[29], C. Padilla[91], S. Paltani[12], F. Pasian[17], K. Pedersen[92], W. J. Percival[93,94,95], V. Pettorino[29], S. Pires[72], G. Polenta[53], M. Poncet[96], L. A. Popa[97], L. Pozzetti[15], F. Raison[58], A. Renzi[98,50], J. Rhodes[64], G. Riccio[25], E. Romelli[17], M. Roncarelli[15], E. Rossetti[20], R. Saglia[60,58], Z. Sakr[99,100,101], D. Sapone[102], B. Sartoris[60,17], M. Schirmer[5], P. Schneider[79], T. Schrabback[103], A. Secroun[51], G. Seidel[5], S. Serrano[55,104,56], P. Simon[79], C. Sirignano[98,50], G. Sirri[21], L. Stanco[50], J.-L. Starck[72], J. Steinwagner[58], P. Tallada-Crespí[31,32], A. N. Taylor[38], H. I. Teplitz[105], I. Tereno[47,106], N. Tessore[70,46], S. Toft[8,11], R. Toledo-Moreo[107], F. Torradeflot[32,31], I. Tutusaus[56,55,100], L. Valenziano[15,54], J. Valiviita[74,75], T. Vassallo[17,57], A. Veropalumbo[14,23,22], Y. Wang[105], J. Weller[60,58], G. Zamorani[15], F. M. Zerbi[14], E. Zucca[15], J. Martín-Fleitas[108], V. Scottez[87,109], and M. Viel[16,17,19,18,110]

(Affiliations can be found after the references)

January 26, 2026

ABSTRACT

We present a search for $z \simeq 7$ Lyman-break galaxies using the 1.72 deg^2 near-infrared UltraVISTA survey in the COSMOS field, reaching 5σ depths in Y of 26.2. We incorporate deep *Euclid* optical and *Euclid* + *Spitzer* NIR imaging for a full spectral energy distribution (SED) fitting analysis. We find 289 candidate galaxies at $6.5 \leq z \leq 7.5$ covering $-22.6 \leq M_{\rm UV} \leq -20.2$, faint enough to overlap with *Hubble* Space Telescope studies. We conduct a separate selection by including complementary *Euclid* performance verification imaging (reaching 5σ depths of 26.3), yielding 140 galaxies in 0.65 deg^2, with 38 sources unique to this sample. We compute the rest-frame UV luminosity function (UV LF) from our samples, extending below the knee ($M^* = -21.14^{+0.28}_{-0.25}$). We find that the shape of the UV LF is consistent with both a Schechter function and double-power law (DPL) at the magnitudes probed by this sample, with a DPL preferred at $M_{\rm UV} < -22.5$ when bright-end results are included. The UltraVISTA+*Euclid* sample provides a clean measurement of the LF due to the overlapping near-infrared filters identifying molecular absorption features in the SEDs of ultra-cool dwarf interlopers, and additional faint galaxies are recovered. A comparison with JWST LFs at $z > 7$ suggests a gentle evolution in the bright-end slope, although this is limited by a lack of robust bright-end measurements at $z > 9$. We forecast that in the Euclid Deep Fields, the removal of contaminant ultra-cool dwarfs as point sources will be possible at $J_{\rm E} < 24.5$. Finally, we present a high-equivalent-width Lyman-α emitter candidate identified by combining HSC, VISTA, and *Euclid* broadband photometry, highlighting the synergistic power these instruments will have in the Euclid Auxiliary Fields for identifying extreme sources in the Epoch of Reionisation.

Key words. Galaxies: high-redshift, Galaxies: luminosity function, Galaxies: evolution, Galaxies: photometry

1. Introduction

A central goal of astrophysics is to unveil the formation and evolution of the first galaxies in the Universe (Stark 2016; Adamo et al. 2025). The luminosity function (LF), or number density of

⋆ This paper is published on behalf of the Euclid Consortium
⋆⋆ e-mail: rohan.varadaraj@physics.ox.ac.uk

galaxies as a function of luminosity/magnitude, is a key statistic for this. In particular, at high-redshift ($z > 5$), observations of rare, luminous galaxies at the bright end ($L > L^*$) of the UV LF provide key insight into astrophysical effects such as feedback and dust build-up (e.g. Bowler et al. 2015; Finkelstein & Bagley 2022; Nikopoulos & Dayal 2024; Algera et al. 2026). Degree-scale ground-based imaging has been central to discovering and characterising these rare, luminous Lyman-break galaxies (LBGs), so-called because of their strong redshifted Lyman-α spectral break at $\lambda_{\rm rest} = 1216$ Å (Guhathakurta et al. 1990; Steidel et al. 1996). Near-infrared (NIR) ground-based surveys such the Ultra Deep Survey (UDS) field of the UKIRT Infrared Deep Sky Survey (UKIDSS, Lawrence et al. 2007) and UltraVISTA (McCracken et al. 2012) enabled the means to discover rare $L > L^*$ LBG candidates at $z > 5$ (McLure et al. 2009; Bowler et al. 2012). Subsequent ground-based studies have confirmed a double-power law (DPL) LF with little evolution in the bright end at $z = 6$–10 (Bowler et al. 2014; Ono et al. 2018; Stefanon et al. 2019; Bowler et al. 2020; Harikane et al. 2022; Kauffmann et al. 2022; Donnan et al. 2023; Varadaraj et al. 2023, hereafter V23). The *Hubble* Space Telescope (HST) has placed strong complementary constraints on the faint end ($L < L^*$, McLure et al. 2013; Finkelstein et al. 2015, hereafter F15; Bouwens et al. 2021, hereafter B21). However, both ground-based telescopes and HST can only probe out to $\lambda = 2\,\mu$m, placing a barrier at $z = 10$. The unparalleled NIR capabilities of JWST substantially advanced the redshift frontier, revealing an abundance of luminous blue galaxies and a markedly slow evolution of the UV LF over the redshift range $z = 10$–14 (e.g. Donnan et al. 2023; McLeod et al. 2024; Adams et al. 2024; Chemerynska et al. 2024; Whitler et al. 2025; Harikane et al. 2025). This has invoked scenarios such as increased star-formation efficiency or Pop. III stars (Harikane et al. 2023a), ejection of dust by radiation-driven outflows (Ferrara et al. 2023), and even tension with ΛCDM (Labbé et al. 2023). The star-formation histories (SFHs) of some luminous $z \simeq 7$ sources can require substantial star formation at $z > 9$ (e.g. Whitler et al. 2023). This, combined with the slow evolution of the LF, means it is natural to return to the most massive, luminous sources at $z \simeq 7$ in order to understand their connection to bright JWST galaxies at $z > 10$.

The study of $z \simeq 7$ sources hinges on the ability to robustly detect them and remove interloper sources. A major issue facing ground-based studies at $z \simeq 7$ has been contamination by Galactic M-, L-, and T-type ultra-cool dwarfs (UCDs, e.g. Stanway et al. 2008; Bowler et al. 2012; Wilkins et al. 2014). These sources have high number densities at the typical apparent magnitudes of $L > L^*$ LBGs, often matching or even exceeding the number of LBG candidates in most degree-scale extragalactic surveys (Ryan et al. 2011). The same molecular species responsible for making the Earth's atmosphere opaque at certain wavelengths in the NIR are also present in UCD atmospheres, causing deep molecular absorption complexes at wavelengths impossible to probe from the ground. This means that in certain cases the NIR photometry of a UCD can be confused with a flat rest-UV LBG continuum. Furthermore, while luminous $z \simeq 7$ LBGs are generally marginally resolved (Bowler et al. 2017, hereafter B17), atmospheric seeing often prevents distinguishing UCDs from LBGs based on their morphology.

The launch of *Euclid* signals the first time astronomers have had access to degree-scale, space-based NIR imaging. *Euclid* is a European Space Agency medium-class mission launched in July 2023, equipped with a 1.2 m primary mirror (Euclid Collaboration: Mellier et al. 2025). Its main goal is to probe dark matter and dark energy through weak lensing and galaxy clustering, with a significant focus also on non-cosmological science. The Visible Camera instrument on *Euclid* (VIS, Euclid Collaboration: Cropper et al. 2025) features a high-resolution (0.″16 FWHM) optical filter, $I_{\rm E}$, equivalent to the ground-based *riz* filters. The Near-Infrared Spectrometer and Photometer (NISP, Euclid Collaboration: Jahnke et al. 2025) features three NIR filters, $Y_{\rm E}$, $J_{\rm E}$, and $H_{\rm E}$, which can probe NIR wavelengths inaccessible from the ground (see Fig. 1). The field of view of *Euclid* is 0.55 deg^2, and the main survey will eventually map out 14 000 deg^2 of the extragalactic sky (Euclid Collaboration: Mellier et al. 2025). The Early Release Observations (EROs, Cuillandre et al. 2025) have led to the identification of the first *Euclid*-selected $z > 6$ LBG candidates (Atek et al. 2025; Weaver et al. 2025), with the very deep $I_{\rm E}$ filter allowing for the removal of M-dwarfs and low-redshift galaxy interlopers by requiring a strong break in $I_{\rm E} - Y_{\rm E}$. However, due to the availability of only four relatively wide photometric filters, and the fact that the NISP images in the ERO reduction have a pixel scale of 0.″3 pix^{-1} meant there were probably still high-levels of contamination by L- and T-type dwarfs.

Euclid will dedicate approximately 10% of its observing time to imaging the Euclid Deep Fields (Euclid Collaboration: Scaramella et al. 2022; Euclid Collaboration: Mellier et al. 2025), covering 53 deg^2 to depths of around 26. The resulting imaging will represent an approximately 30-fold increase in area compared to previous NIR surveys reaching this depth (UltraVISTA, McCracken et al. 2012). The considerably wider area will lead to the discovery of thousands of $z \simeq 7$ galaxies brighter than $m_{\rm AB} = 26$ (B17), allowing for definitive measurements of the bright end of the UV LF. Until the Euclid Deep Survey is complete, early imaging from the Euclid Auxiliary Fields (EAFs), used for calibration and reaching depths comparable to the EDFs, serves as an ideal test bed for selecting high-redshift galaxies with *Euclid*. In the COSMOS field, by combining NISP with complementary NIR photometry from VISTA, it may be possible to break the degeneracy between the colours of L- and T-type dwarfs and genuine high-redshift LBGs. The construction of pure $z \simeq 7$ samples is critical because there is still some tension between ground-based studies, which suggest a shallower decline in the bright-end akin to a DPL (Bowler et al. 2014; B17; Harikane et al. 2022; V23), and the widest-area HST-based study of B21 who find a marked drop in the LF between $M_{\rm UV} = -21.5$ and $M_{\rm UV} = -22$, suggesting an exponential decline. The final data release of the NIR UltraVISTA survey, covering 1.72 deg^2 in the COSMOS field at $\lambda = 1$–$2.5\,\mu$m, provides the necessary depth to connect ground-based observations with space-based observations at the knee of the LF, and its combination with *Euclid* imaging provides the means to construct clean samples of UltraVISTA-selected galaxies. Furthermore, with the higher resolution of *Euclid* we can resolve luminous ground-selected sources for the first time without the need for dedicated follow-up imaging from HST (B17; Stefanon et al. 2017). This could allow the removal of UCDs as point sources (and perhaps even through proper motion) and will unveil the morphologies of thousands of galaxies at $z > 6$.

This paper is structured as follows. In Sect. 2, we describe the ground-based and space-based imaging used in this work, as well as the image preparation and photometric catalogue construction. Section 3 outlines the selection of our LBG candidates using SED fitting. For the SED fitting we conduct two separate selections with/without the additional *Euclid* photometry. We present each of our UltraVISTA-only and UltraVISTA+*Euclid* samples in Sect. 4, and we compute the UV LF at $z \simeq 7$ in Sect. 5, comparing our results with JWST measurements of the UV

LF at $z > 7$. Then, in Sect. 6 we discuss the improved SED constraints with *Euclid*, investigate the ability of *Euclid* to remove UCDs as point sources, and highlight the unique capabilities of several overlapping filters to identify extreme Lyman-α emitters. Finally, we conclude and summarise in Sect. 7. The uncertainties presented in this paper denote $\pm 1\,\sigma$ uncertainties where Gaussian, or enclose 68.3% of the data when the underlying distribution is asymmetric. All magnitudes are reported in the AB system (Oke & Gunn 1983). We assume a standard cold dark matter cosmology, $H_0 = 70\,\mathrm{km\,s^{-1}\,Mpc^{-1}}$, $\Omega_\mathrm{m} = 0.3$, $\Omega_\Lambda = 0.7$.

2. Data and image processing

In this section we present the ground- and space-based data used in this work, and the steps taken to prepare the images for creating catalogues and conducting a high-redshift galaxy selection.

2.1. Ground-based imaging and Spitzer

We make use of extensive multi-wavelength imaging in the COSMOS field (Scoville et al. 2007). The UltraVISTA survey (McCracken et al. 2012) is an ultra-deep NIR survey covering $1.72\,\mathrm{deg^2}$ at $\lambda = 1$–$2.5\,\mu$m, vital for characterising the UV continuum of high-redshift LBGs. Data Release 6 (DR6, see Dunlop et al. 2023 for an overview), the final data release[1], provides uniform depths across the full area, bringing the 'deep' stripes up to the same depth as the 'ultradeep' stripes ($5\,\sigma$ depths in Y of 26.2, see Section 2.5). These stripes differed in depth in previous data releases, effectively halving the available ultradeep area. The footprint of the UltraVISTA survey is shown in Fig. 2. Deep optical data are available from the Hyper Suprime-Cam Subaru Strategic Program DR3 (HSC-SSP, Aihara et al. 2022) in the *grizy* bands at $\lambda = 0.4$–$1\,\mu$m. The HSC-SSP data cover the full UltraVISTA footprint. This deep optical imaging is critical for ensuring non-detections bluewards of the Lyman break, where flux bluewards of 1216 Å (rest-frame) is absorbed by neutral hydrogen in the intergalactic medium. HSC-SSP also provides two narrowband filters, namely NB0816 and NB0921, powerful for reducing uncertainties in photometric redshifts (in combination with i, z, and y for constraining the break position, and for detecting Lyman-α with NB0921 at $z = 6.57$). The HSC and VISTA filter widths and wavelength coverage are shown in Fig. 1. Additionally, infrared data from *Spitzer*/IRAC are available as part of the Cosmic Dawn Survey (DAWN, Euclid Collaboration: Moneti et al. 2022) which takes data from S-COSMOS (Sanders et al. 2007) and SMUVS (Ashby et al. 2018) in the $3.6\,\mu$m and $4.5\,\mu$m filters. These lie beyond the Balmer break of $z \simeq 7$ galaxies, providing a measurement of their rest-frame optical flux. The depths of the imaging (measured in Sect. 2.5) in the above filters are presented in Table 1.

2.2. Euclid

We make use of performance verification (PV) imaging, taken for calibration of the instrument, in the COSMOS field over three months. The imaging used in this work is the result of 184 individual exposures in a single observation. Each observation is composed of six exposures for VIS (four long exposures separated on the sky by the dither pattern and two short exposures on two of the dithers) and four exposures for NISP. The calibration involves computing the astrometric solution using *Gaia* DR3 (Gaia Collaboration et al. 2023), flat fielding, and photometric calibration. These calibrated frames are then background-subtracted, coadded and split into mosaics with common astrometry and pixel scale ($17' \times 17'$ for the EDFs and EAFs with $0\farcs1\,\mathrm{pix^{-1}}$). After just a few months of operations, the *Euclid* imaging in COSMOS reaches deeper limiting magnitudes than the UltraVISTA survey, which was conducted over nearly 15 years. The *Euclid* imaging covers $0.65\,\mathrm{deg^2}$ of the UltraVISTA footprint, as shown in Fig. 2. The NISP Y_E, J_E, and H_E bands are 0.2–0.6 mag deeper than their VISTA counterparts. Additionally, the high-resolution I_E filter from the VIS instrument, which covers the same wavelengths as HSC r, i, and z, is 0.3–1.0 mag deeper than these filters. We show the *Euclid* filter widths and wavelength coverage in Fig. 1. The depths of the *Euclid* imaging are presented in both Table 1 and Fig. 1. We do not use data from the NISP spectroscopic channel (NISP-S, grism spectroscopy) since these sources are too faint for spectral extraction by the SIR pipeline ($H_\mathrm{E} < 22.5$ is currently required).

2.3. Image preparation

We follow a similar procedure as in V23. The UltraVISTA data are matched to the *Gaia* EDR3 reference catalogue (Gaia Collaboration et al. 2021). We use `Scamp` (Bertin 2006) and `Swarp` (Bertin et al. 2002) to shift all other auxiliary data into the same frame as the UltraVISTA imaging. The *Euclid* 'MER' (merged) mosaics imaging over the UltraVISTA field consist of 23 of the $17' \times 17'$ tiles. `Swarp` was also used to resample the *Euclid* images to match the pixel scale of UltraVISTA, $0\farcs15\,\mathrm{pix^{-1}}$, and to produce one large mosaic for each *Euclid* image matching the plate scale of UltraVISTA.

2.4. PSF homogenisation

In the ground-based seeing-dominated imaging, sources tend to be close to unresolved (PSF FWHM = $0\farcs8$). The differences in PSF between VISTA and *Euclid* and the possibility of sources being both resolved and unresolved depending on the instrument means that the fraction of flux falling within a fixed-size aperture depends strongly on the filter. We therefore homogenise all of the space-based imaging to match the VISTA Y band PSF, chosen since it is the main detection band for $z \simeq 7$ LBGs and because it has the largest PSF of VISTA. We use `PSFEx` (Bertin 2011) to construct an empirical PSF model. Stars are selected from the magnitude-FWHM diagram, with FWHMs determined by `SExtractor` (Bertin & Arnouts 1996). We use `PyPher` (Boucaud et al. 2016) to find the convolution kernel between the *Euclid* PSFs and the VISTA Y band PSF. The space-based images are convolved with this kernel, leading to PSF-homogenised images that are pixel-matched to UltraVISTA. We rerun `PSFEx` (Bertin 2011) on the homogenised images using the same stars selected in the original *Euclid* images. The new PSF model is used to determine the enclosed flux within a $1\farcs8$ diameter circular aperture, assuming a point source.

Prior to PSF homogenisation, the FWHMs of the *Euclid* PSFs are $0\farcs20$ in I_E, $0\farcs49$ in Y_E, $0\farcs51$ in J_E, and $0\farcs53$ in H_E, as measured with `PSFEx`. These values are in agreement with PSF FWHMs measured by the *Euclid* pipeline. After homogenisation of the *Euclid* images, all PSF FWHMs match that of VISTA Y, $0\farcs85$. We note that all *Euclid* postage stamp cutouts presented in this work are from the original images, prior to PSF homogenisation. We then check the PSF-homogenised *Euclid* photometry to ensure it is consistent with UltraVISTA. This is

[1] https://eso.org/rm/api/v1/public/releaseDescriptions/221

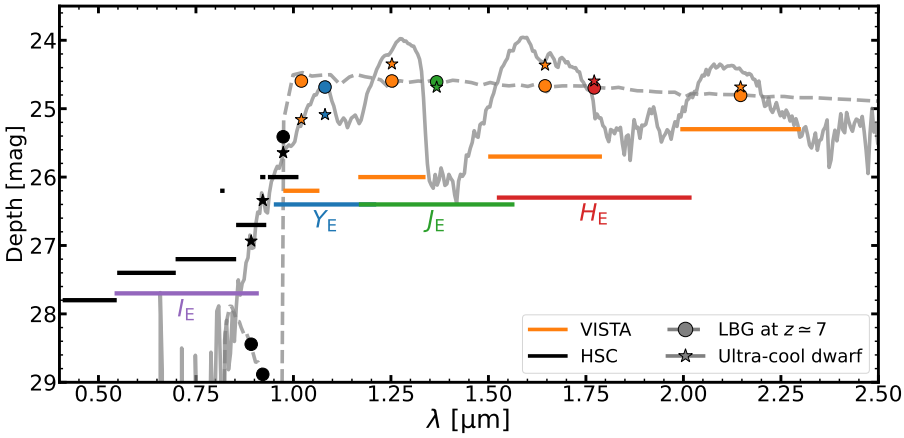

Fig. 1. Limiting magnitudes, or modal depths ($5\,\sigma$) of the photometric filters used in this work within the COSMOS field. The line widths represent the FWHM of the filter transmission curves, and the depths are reported in Table 1. The HSC and VISTA filters are shown in black and orange, respectively, and the four *Euclid* filters are labelled. We also show example SEDs of a UCD and a LBG with the solid and dashed lines, respectively. The model photometry for the UCD and the LBG are shown by the stars and circles respectively, and are colour-coded by their filters. Note that the *Euclid* NIR filters cover the gaps between the VISTA filters. These wavelengths are inaccessible from the ground due to the atmospheric absorption.

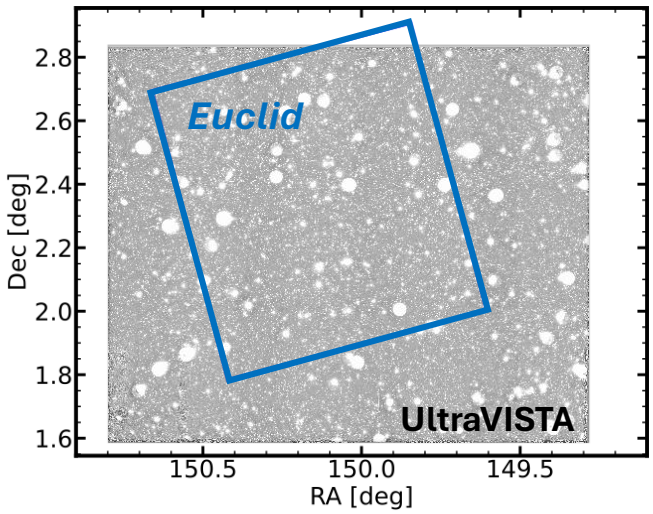

Fig. 2: The COSMOS UltraVISTA (McCracken et al. 2012) footprint with the *Euclid* COSMOS PV footprint overlaid. Optical imaging from HSC-SSP DR3 (Aihara et al. 2022) covers the full UltraVISTA area. The overlapping area between *Euclid* and UltraVISTA covers 0.65 deg^2.

Table 1: The $5\,\sigma$ limiting magnitudes for each band used in this work in the COSMOS field.

Filter	Depth ($5\,\sigma$)	Instrument
g	27.8	HSC
r	27.4	HSC
i	27.2	HSC
NB0816	26.2	HSC
z	26.7	HSC
NB0921	26.0	HSC
y	26.0	HSC
Y	26.2	VISTA
J	26.0	VISTA
H	25.7	VISTA
K_s	25.3	VISTA
I_E	27.7	*Euclid*
Y_E	26.4	*Euclid*
J_E	26.4	*Euclid*
H_E	26.3	*Euclid*
3.6	25.2	*Spitzer*/IRAC
4.5	25.2	*Spitzer*/IRAC

Notes. The local depths were measured by placing 1.″8 diameter circular apertures on empty regions of the images. The depth quoted here is the mode of these local depths. Depths for *Euclid* were measured on images pixel-matched and PSF-homogenised to the VISTA Y band. IRAC depths were measured in 2.″8 diameter circular apertures on the original resolution image to account for the poorer resolution.

done by taking the stars selected in Sect. 2.4 and imposing the cut $|Y-J| < 0.05 \wedge |J-H| < 0.05$ to obtain stars with flat colours across the VISTA YJH bands. We then check the colour of each *Euclid* filter and its nearest VISTA counterpart. This check is shown in Appendix A. Just as with the VISTA photometry, a minimum uncertainty of 5% is placed on the *Euclid* photometry. There are no large colour differences between *Euclid* and VISTA filters for stars with flat NIR colours, indicating that there are no major zeropoint or flux calibration issues in the *Euclid* COSMOS imaging.

2.5. Depths

We computed $5\,\sigma$ depths across the images by placing roughly 2×10^6 apertures with diameters of 1.″8 on empty regions of the image (determined using the `SExtractor` segmentation map). For the *Spitzer*/IRAC images we use a 2.″8 diameter circular aperture to account for the broader PSF. We determine local depth maps by taking the closest 300 apertures to each point and measuring the median absolute deviation of the aperture fluxes. The depths reported in Table 1 are the mode of the local depths.

The depths of the PSF homogenised *Euclid* images match the depths of the original image.

2.6. Catalogues

We run `SExtractor` in dual image mode on a VISTA $Y + J$ stacked image, using the same parameters as in V23. Photometry was performed in a 1.″8 diameter circular aperture, enclosing 70–80% of the total flux assuming a point source. This balances between a high signal-to-noise ratio whilst preventing the need for a large aperture correction. We use 2.″8 diameter circular apertures for *Spitzer*/IRAC to account for its broader PSF, enclosing a similar fraction of the total flux. The raw aperture flux measurements must be corrected to account for light falling outside of the aperture in order to obtain a measure of the total flux. As discussed in Sect. 2.4, we use `PSFEx` to determine a PSF model with stars selected from the FWHM vs. MAG_AUTO diagram. This

empirical model is used to measure the flux enclosed in a 1.″8 diameter aperture (or 2.″8 for *Spitzer*/IRAC), providing the PSF correction. A minimum uncertainty of 5% is placed on photometry in all bands. We note that for extended sources, aperture photometry may underestimate the total flux. To check this, we compare our aperture fluxes to MAG_AUTO measurements from `SExtractor`, which uses flexible elliptical apertures to measure the total flux (Kron 1980). We find that the aperture photometry can underestimate the total flux by around 0.1 mag, consistent with a similar analysis conducted in (Bowler et al. 2014; B17). We scale the SEDs by the ratio between MAG_AUTO and the aperture photometry before measuring quantities which rely on the SED, such as $M_{\rm UV}$ and $V_{\rm max}$ (see Sects. 4 and 5.2). When creating the catalogues, we also mask regions of low signal-to-noise and bright stars in the UltraVISTA images. This is accounted for in the field area of 1.72 deg^2.

3. Candidate selection

In this section we outline the methods used to select the $z \simeq 7$ candidates. We conduct two different selections.

1. The UltraVISTA-only selection (U-only): we run the SED fitting steps with the HSC+VISTA+*Spitzer*/IRAC photometry, without *Euclid*.
2. The UltraVISTA+*Euclid* selection (U+E): we add in the *Euclid* photometry for the SED fitting and visual selection steps.

We stress that the sample is still UltraVISTA-selected, since sources are first selected based on their VISTA photometry (see Sect. 3.1). By keeping the selection based on ground-based imaging, we avoid the introduction of artefacts from *Euclid*, such as persistence (see Weaver et al. 2025). Persistence is an issue for LBG searches at $z > 6$ since it only appears in NISP, masquerading as a VIS-dropout source. Additionally, selecting from the shallower VISTA imaging usually ensures a detection in the deeper *Euclid* imaging.[2] The *Euclid* photometry is therefore providing additional information for the SED fitting of an UltraVISTA-selected sample. In both selections, ancillary HSC and *Spitzer* data are also used. The HSC data are used to assert non-detections bluewards of the Lyman break, and if unconfused, the *Spitzer*/IRAC data are used to remove low-redshift contaminants, which generally show redder slopes at these wavelengths than LBGs (see Sect. 3.4).

In the following sections, we outline the steps for the U-only sample. Then, in Sect. 3.5, we present the U+E SED fitting, highlighting the differences in the selection steps from the U-only sample. The selection steps and number of sources removed at each step for both selections are shown in Table 2.

3.1. Initial selection

Objects are first selected by requiring that they are sufficiently bright in the detection filters. We impose a $5\,\sigma$ detection threshold in $Y + J$, which removes roughly one third of the sources in the catalogue (see Table 2). We then require non-detections ($< 2\,\sigma$ significance) in the HSC g, r, and i bands. No condition is imposed on HSC z, since the Lyman-break can enter this filter towards the lower end of the redshift range $6.5 \leq z \leq 7.5$. These non-detection conditions reduce the catalogue from 1 051 995 to 4849 objects. We again stress that this first selection is for a base UltraVISTA sample, without using *Euclid* data.

3.2. SED fitting

We use all ground-based filters available to conduct an SED fitting analysis in order to identify LBG candidates at $z \simeq 7$. In general, SED fitting is more complete than a colour-colour selection (Adams et al. 2020), although it can introduce a more complex selection function because it depends on the adopted templates and on degeneracies between them, particularly at low signal-to-noise. We use the `LePhare` SED fitting code (Arnouts et al. 1999; Ilbert et al. 2006), which minimises χ^2 to find the best-fitting photometric redshifts and SEDs. Following V23, we use Bruzual & Charlot (2003) stellar population models with metallicities of $Z \in \{0.2, 0.4, 1.0\}\,Z_\odot$. The star-formation histories used are constant, instantaneous bursts, and exponentially declining with time-scales ranging from $\tau = 0.05$–10 Gyr. Uniform priors are placed on the following parameters. The redshift was allowed to vary between $z = 0$–9. Stellar population ages are allowed to vary between 10 Myr and 13.8 Gyr, limited by the age of the Universe at a given redshift. We use the Calzetti et al. (2000) attenuation law, allowing $A_V = 0.0$–4.0, a Chabrier (2003) initial mass function is assumed, and intergalactic medium absorption is applied according to Madau (1995). We initially only use HSC+VISTA to determine photometric redshifts, excluding *Spitzer*/IRAC since the rate of non-detections increases in the faint end of the sample due to the shallower depth, and to make the completeness analysis more consistent. For example in the final U+E sample, at $Y < 25.5$, 17 out of 18 sources have an IRAC detection of at least $2\,\sigma$. However, at $Y > 25.5$ this drops to around half of the sources. The main constraining power of *Spitzer*/IRAC in this work is to therefore remove bright low-redshift dusty galaxy interlopers. It is used later in Sect. 3.4, in cases where there is no confusion.

Lyman-α emission can provide additional flux to the broad-band photometry, acting to increase the photometric redshifts of objects by up to $\Delta z \sim 0.5$ (Bowler et al. 2014). To account for this, we also add Lyman-α emission lines to the Bruzual & Charlot (2003) templates with equivalent widths $0 \leq {\rm EW}_0\,/\text{Å} \leq 240$ by measuring the continuum level in the range $\lambda = 1250$–1300 Å.

Based on the best-fit galaxy templates, candidates are first required to have their photometric redshift $z > 6$. The fits then had to be sufficiently good. Given the five degrees of freedom in the SED fitting, a $2\,\sigma$ significance threshold corresponds to $\chi^2 < 11.3$. Additionally, we require that the high-redshift solution is preferred to the low-redshift solution with $2\,\sigma$ significance, corresponding to $\Delta\chi^2 > 4$ between the two solutions. Single-band detections are also removed since they do not present robust candidates. We show the model photometry of an example LBG in Fig. 1.

3.3. Visual inspection

We carry out a visual selection of the remaining objects to remove artefacts. These artefacts are typically diffraction spikes and cross-talk in the UltraVISTA images. The latter of these artefacts is caused during the readout from the Vista InfraRed CAMera (VIRCAM) instrument, producing ghost images at regular pixel intervals from bright stars (see Kauffmann et al. 2022). We use a catalogue of bright stars selected from the UltraVISTA

[2] Sources detected in VISTA but not in *Euclid* are usually located in regions where the *Euclid* imaging is shallower than VISTA, for example near the edges of the *Euclid* footprint. However, the possibility of extremely high proper motion cannot be excluded.

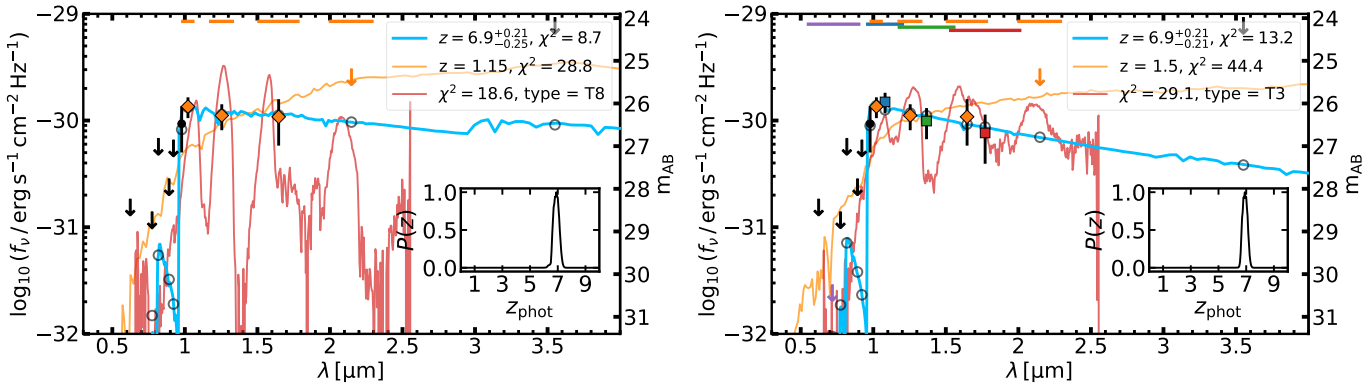

Fig. 3: SED fitting of a candidate LBG, EUCL J100041.40+020157.5 (hereafter LBG 10004+02015), at $z = 6.90$. Additional candidates are presented in Appendix C. *Left*: the SED fitting without *Euclid* data, as part of the U-only selection (see Sect. 3). *Right*: the SED fitting including *Euclid* data, as part of the U+E selection. The HSC, VISTA and *Euclid* photometry are shown by the points, diamonds and squares, respectively. The photometry is coloured following Fig. 1. Non-detections are replaced with $2\,\sigma$ upper limits. We also show the filter widths for VISTA and *Euclid* at the top of the plot. The *Spitzer*/IRAC model photometry and upper limit in the 3.6 μm filter is also shown. The blue curve shows the best high-redshift solution, and the grey open circles are its expected model photometry. The orange curve shows the best dusty low-redshift solution, and the red curve shows the best UCD solution. The legend in the top right shows the redshift and χ^2 of the galaxy solutions, and the χ^2 and spectral type of the UCD solution. The inset panel shows the redshift probability distribution for this source. The inclusion of *Euclid* data reinforces the exclusion the UCD solution. Also note that the inclusion of *Euclid* data prefers a bluer slope.

Table 2: Number of sources remaining in our catalogues after each selection step, beginning from the initial VISTA $Y + J$-selected catalogue.

Selection step	Objects remaining	
Initial catalogue	1 051 995	
$5\,\sigma$ $Y + J$ VISTA cut	706 607	
$< 2\,\sigma$ in HSC g	32 165	
$< 2\,\sigma$ in HSC r	13 212	
$< 2\,\sigma$ in HSC i	4849	
SED fitting step	UltraVISTA-only	UltraVISTA+*Euclid*
Overlap with *Euclid*	—	1850
Initial $z > 6$ cut	1872	403
Visual selection	751	341
Low-z: $\chi^2_{\mathrm{low-z}} < \chi^2_{\mathrm{high-z}} + 4$	718	333
UCDs: $\chi^2_{\mathrm{UCD}} < \chi^2_{\mathrm{high-z}}$	656	315
$6.5 \leq z_{\mathrm{phot}} \leq 7.5$, with Ly$\alpha$	289	140

Notes. The first column shows the selection step. The second column shows the number of objects remaining. For the SED fitting steps (and the visual selection), we conduct two different selections: the U-only selection, where *Euclid* photometry is not included, and the U+E selection, where *Euclid* photometry is included. In both selections, ancillary HSC and *Spitzer* data are also used as required. For the U+E selection, we restrict the catalogue to the 0.65 deg^2 *Euclid* footprint. The high-redshift ($z > 6$) cut is defined as the best-fitting SED solution having its photometric redshift $z > 6$, $\chi^2 < 11.3$ (U-only) or 17.5 (U+E), and $\Delta\chi^2 > 4$ between the low- and high-redshift solutions.

J band using `SExtractor` to flag potential crosstalk artefacts. This was done by constructing a grid of positions at multiples of 128 pixels from these bright stars, then flagging sources within a conservative 6″ radius of these positions. At the magnitudes probed in this work, the crosstalk artefacts usually appear more diffuse and extended compared to real sources, and the visual presence in either HSC z or *Spitzer*/IRAC, which do not suffer from cross-talk, is a clear signpost for a real object. We create an optical stack from HSC g, r, and i to check for low-level flux indicative of a low-redshift galaxy. We also smooth the optical stack with a Gaussian filter with $\sigma = 2$ pixels, which helps in searching for low-level flux. Crosstalk artefacts are numerous in the deep UltraVISTA data, leading to the removal of 60% of sources.

3.4. Removing interlopers

There are two primary classes of low-redshift interloper objects that act to contaminate $z \simeq 7$ LBG samples – dusty low-redshift galaxies and UCDs. Dusty galaxies at $z \sim 1$–2 can have Balmer breaks that can be confused as Lyman breaks. However, these galaxies tend to have SEDs that increase in flux rapidly towards longer wavelengths (see e.g. Rodighiero et al. 2010; Le Bail et al. 2024). Additionally, a Lyman break is usually stronger than the Balmer break, which tends to have shallower slope (see the dusty low-redshift galaxy model in Fig. 3). If the SED fitting prefers a low-redshift solution to the $z > 6$ solution when the *Spitzer*/IRAC imaging is included and unconfused at $2\,\sigma$ significance ($\Delta\chi^2 > 4$), the object is removed.

UCDs of spectral type M, L, and T have SEDs featuring very little blue optical flux and heavy molecular absorption complexes (see e.g. Burgasser et al. 2024 and Luhman et al. 2024 for recent JWST spectroscopic observations). These sources

present a pressing challenge for ground-based searches since the peaks of the UCD SEDs usually coincide with the VISTA $YJHK_s$ filters, mimicking a flat NIR colour that can be confused with a blue $z \simeq 7$ UV continuum. This occurs because the molecular species responsible for the absorption complexes (e.g. CH_4, H_2O) are the same species responsible for making Earth's atmosphere opaque at certain wavelength ranges in the NIR (e.g. Bailey et al. 2007). We use UCD templates taken from the SpeX prism library (Burgasser 2014) for the SED fitting, covering spectral types M4 through to T8, with one template per spectral type. We exclude the HSC g and r bands from this fitting since the templates do not contain any information at these wavelengths. We remove sources with $\chi^2_{\rm UCD} < \chi^2_{\rm high-z}$, meaning the UCD fit is preferred to the high-redshift solution. In Fig. 1, we show the model photometry for an example UCD template, and compare it to the model photometry for an LBG to highlight the differences in the expected photometry.

We retain sources with a redshift $z < 6.5$ when fitted without the Lyman-α emission line, but fall within our redshift range when the line is included and it provides the best fit (see Sect. 3.2). Finally, we restrict the redshift of candidates to $6.5 \leq z \leq 7.5$, removing 55% of sources, which lie at $6.0 \leq z < 6.5$.

3.5. Redoing the SED fitting with Euclid

We then rerun the SED fitting by combining *Euclid* with VISTA on the remaining objects after the initial photometric selection (Sect. 3.1). When the 4849 objects from this step are constrained to within the 0.65 deg^2 *Euclid* footprint, there are 1850 remaining. The additional four filters change the χ^2 cut we impose for the initial high-redshift selection in Sect. 3.2, increasing this to $\chi^2 < 17.5$. This initial high-redshift cut with *Euclid* photometry removes many more objects than the same step without *Euclid* photometry. This is because VISTA artefacts have non-detections in *Euclid*, leading to poor SED fits. Following on from this, the *Euclid* imaging is also extremely powerful for the visual check – existence of a source in both *Euclid* and VISTA immediately confirms it as real, and not an artefact. Such a technique may also be used in reverse for future studies that use VISTA+*Euclid* imaging – selections based on *Euclid* can use VISTA to rule out common artefacts such as ghosts and persistence. Similarly, Weaver et al. (2025) leverage *Spitzer*/IRAC detections to rule out artefacts. The results of the selection steps after incorporating *Euclid* photometry for the SED fitting and visual selection are also shown in Table 2.

3.6. Expected number of ultra-cool dwarfs

Using the model from Bowler et al. (2015) of a single exponential disc with a scale height of 300 pc, we expect that there will be around 800 UCDs (of spectral type M4 through to T8) brighter than the initial 5 σ cut in the full UltraVISTA field. For the U-only selection, the UCD removal step removes 62 objects, which is fewer than expected. However, prior to the initial high-redshift cut, of the 4849 objects there are 1372 objects with a best-fitting UCD SED. The increased number with respect to the expected amount is likely to be caused by upscattering of UCDs into the selection, some faint galaxies being misidentified as UCDs, and crosstalk artefacts which had not yet been removed in a visual selection.

Restricting to the *Euclid* footprint for the U+E selection, we expect around 250 UCDs. The UCD removal step cuts only 18 objects. Prior to the initial high-redshift cut, there are 205 objects with a best-fitting UCD SED. The total is very close to the expected number. The *Euclid* photometry improves constraints via SED fitting (see Sect. 6.1), and *Euclid* non-detections immediately rule out VISTA crosstalk artefacts, explaining the elevated number of objects with best-fit UCD SEDs in the U-only selection (relative to the prediction).

In V23, which used 8.2 deg^2 of imaging from the VISTA Deep Extragalactic Observations survey (VIDEO, Jarvis et al. 2013), reaching 5 σ depths in Y of 25.2, a large fraction (80%) of high-redshift candidates were identified as possible UCDs, since sources sampled the magnitude range $24.1 \leq J \leq 25.2$ where the surface density of UCDs is much higher than that of LBGs (Ryan et al. 2011). UltraVISTA is a magnitude deeper than VIDEO, and the sample in this work probes down to $J = 26$ where the UCDs do not outnumber LBGs as substantially. We note that the number of sources best fit as UCDs that make it through the initial high-redshift cut (62 for U-only, 18 for U+E) is significantly smaller than the final sample of LBGs (see Table 2), showing that UCD contamination is not as severe as in V23, but still a large issue.

4. Candidate galaxies

The final U-only sample consists of 289 candidates selected from 1.72 deg^2 of UltraVISTA imaging. We show the SED fitting of an example galaxy, LBG 10004+02015, in Fig. 3. Additional candidates are presented in Appendix C. We measure the absolute rest-frame UV magnitude, $M_{\rm UV}$, by placing a top-hat filter on the best-fit SED at 1500 Å, with width 100 Å. The sample spans a range of over two magnitudes, $-22.5 \leq M_{\rm UV} \leq -20.2$. Their distribution in $M_{\rm UV}$ and photometric redshift $z_{\rm phot}$ is shown in Fig. 4. The brightest candidates in our sample have similar $M_{\rm UV}$ to the fainter sources in V23, where we used 8.2 deg^2 of shallower ($m_{\rm AB} \sim 25$) imaging to select ultra-luminous $z \simeq 7$ candidates. Of course, due to the smaller area of UltraVISTA, our sample does not probe as bright as we could in the wider XMM-LSS and ECDF-S fields, but we are able to select a much fainter sample due to the improved depth. Compared to the previous search for $z \simeq 7$ LBGs in UltraVISTA by Bowler et al. (2014) on DR2 imaging, we find an additional 257 galaxies thanks to the increase in depth by a magnitude, combined with an effective doubling in survey area since the 'deep' stripes have been brought up to the same depth as the 'ultradeep' stripes. UltraVISTA DR6 is also deep enough to reach magnitudes comparable to the bright end of the UV LF presented in B21 (see Fig. 4), the widest-area HST search for LBGs at $z \simeq 7$, bridging the gap between space-based and ground-based observations of the UV LF at this redshift for the first time.

When we include *Euclid* imaging over the 0.65 deg^2 which overlaps with UltraVISTA, for the U+E selection, our sample consists of 140 galaxies. Of these, 102 are also found in the U-only sample. The remaining 38 galaxies are unique to the U+E sample. In Fig. 3, we also show the SED fitting of LBG 10004+02015 when the *Euclid* photometry is included. We show the distribution of the U+E sample in Fig. 4, including the 38 galaxies that are not selected in the U-only sample. These 38 galaxies have $M_{\rm UV}$ largely corresponding to the 40–50% completeness range, showing that the deeper *Euclid* photometry recovers fainter galaxies in the sample. Additionally, of these 38 galaxies, seven lie at $z > 7.2$ with brighter magnitudes, $M_{\rm UV} < -21$, where VISTA photometry is more susceptible to contamination by UCDs and cross-talk artefacts. We present the SED fitting and postage stamp images of the brightest 30 galaxies in the U+E sample in Appendix C. A table of all sources

Table 3: First five rows of the table containing the candidate properties of the U+E sample.

ID	RA [deg]	Dec [deg]	$z_{\rm phot}$	χ^2	$z_{\rm phot,sec}$	$\chi^2_{\rm sec}$	UCD Model	$\chi^2_{\rm UCD}$	EW$_{\rm Ly\alpha}$ [Å]	$M_{\rm UV}$
EUCL J100054.15+015048.3	150.226	1.846	$6.65^{+0.11}_{-0.08}$	8.4	1.45	13.4	M6	12.2	0.0	$-20.43^{+0.08}_{-0.08}$
EUCL J100105.05+015227.0	150.271	1.874	$6.88^{+0.15}_{-0.31}$	6.5	1.50	27.6	M6	21.4	0.0	$-21.02^{+0.09}_{-0.13}$
EUCL J100048.32+015330.8	150.201	1.892	$6.56^{+0.06}_{-0.08}$	10.3	1.45	38.0	T3	22.1	0.0	$-20.92^{+0.07}_{-0.08}$
EUCL J100028.55+015503.9	150.119	1.918	$7.18^{+0.10}_{-0.21}$	14.1	1.55	42.4	T8	21.2	0.0	$-21.08^{+0.08}_{-0.10}$
EUCL J100120.73+015542.5	150.336	1.928	$7.22^{+0.14}_{-0.15}$	7.1	1.55	31.1	T3	21.7	0.0	$-21.23^{+0.08}_{-0.09}$
				⋮						

Notes. The fluxes within 1.″8 diameter circular apertures, along with uncertainties, are also provided in the online version. We also provide the same table for the U-only sample. The first three columns show the ID, RA, and Dec of the source. The next six columns show photometric redshift and χ^2 value of the the LBG solution, as well as the low-redshift dusty galaxy solution, and the stellar type and χ^2 of the UCD solution. The final two columns show the equivalent width of the Lyman-α emission line if a template with the emission line is preferred, and the absolute rest-frame UV magnitude $M_{\rm UV}$.

along with postage stamps of the *Euclid* sources will be provided as online material. We present the first five rows of the U+E sample in Table 3.

In Appendix B and Fig. B.1, we compare the $M_{\rm UV}$ and $z_{\rm phot}$ derived with and without *Euclid*. This is done by comparing the measurements for sources which exist in both the U+E and U-only samples. The photometric redshifts are in strong agreement across both samples. The scatter appears to increase at $z > 6.95$ (although all redshifts are consistent within errors). This redshift corresponds to the blue side of the $Y_{\rm E}$ filter, suggesting that the increased scatter is driven by the improved determination of the position of the break when *Euclid* data is included, driving shifts in the $z_{\rm phot}$ by $\Delta z \sim 0.1$-0.2. Below this redshift, the wide $I_{\rm E}$ filter does not provide significant information on the break position. There is some scatter in the measurements of $M_{\rm UV}$, however the values only shift by up to 0.2 mag. We briefly discuss the impact this has on the LF in Sect. 5.3.

5. The UV LF with UltraVISTA and *Euclid*

In this section we present the calculation of the UV LF at $z \simeq 7$ using both the U-only and U+E samples. We then fit a DPL and Schechter function using the U+E sample, before comparing our results to theoretical predictions at $z \simeq 7$ and JWST determinations of the UV LF at $z > 7$.

5.1. Completeness

Incompleteness of the final galaxy sample must be accounted for before computing the UV LF. Genuine high-redshift galaxies can become blended with other objects, and near the limiting magnitude of the detection images, photometric scattering can cause objects to drop in/out of the selection. We therefore run injection-recovery simulations to derive corrections for these effects in bins of $M_{\rm UV}$ and $z_{\rm phot}$. First, we populate a redshift–absolute-magnitude grid with steps of $\Delta z = 0.05$ and $\Delta M = 0.1$, assuming the DPL LF derived in Harikane et al. (2025). The absolute magnitude grid extends down to $M_{\rm UV} = -19$, well below the limiting magnitude of UltraVISTA DR6, to account for the photometric up-scattering of faint sources. The grid consists of 10^6 sources. Then, we generate mock Y and J photometry. We draw rest-frame UV slopes, $\beta_{\rm UV}$, from a Gaussian distribution centred on $\beta_{\rm UV} = -2$ with standard deviation $\sigma = 0.2$ (Bowler et al. 2014). We inject empirical PSF models (see Sect. 2.4) into the imaging, assuming sources are generally unresolved in ground-based imaging (see Bowler et al. 2014). We inject 10^3 sources at a time into the $Y + J$ image so as to not artificially boost the number density too much. Then, we run `SExtractor` in the same manner as in Sect. 2.6 and select sources using the same cuts. We show the 30, 40, and 50% completeness limits in Fig. 4. The faintest sources in our sample correspond roughly to the 40% contour, below which the completeness drops rapidly.

5.2. The rest-frame UV LF

We use both samples of LBGs (U+E and U-only) to determine the UV LF at $z \simeq 7$ using the $1/V_{\rm max}$ method (Schmidt 1968). $V_{\rm max}$ is the maximum comoving volume in which the galaxy could lie and still fulfil our selection criteria. The galaxy SEDs were redshifted in steps of $\Delta z = 0.01$ until they fell out of the $5\,\sigma$ detection threshold in $Y + J$, giving us its maximum redshift $z_{\rm max}$ at which it would still be detected in our selection. $V_{\rm max}$ is then the comoving volume between $z = 6.5$ and $z = z_{\rm max}$. The value of $z_{\rm max}$ cannot exceed $z = 7.5$, the maximum considered redshift. The UV LF in a given bin of absolute magnitude, $\phi(M)$, in the redshift range $6.5 < z < 7.5$, is then given by

$$\phi(M) = \frac{1}{\Delta M} \sum_{i=1}^{N} \frac{1}{C(M_i, z_i)} \frac{1}{V_{\rm max,i}}\,, \tag{1}$$

where we sum over N galaxies in the magnitude bin with width ΔM. $C(M_i, z_i)$ is the completeness value for the galaxy in its magnitude and redshift bin, calculated in Sect. 5.1. We assume uncertainties are Poissonian, given by

$$\delta\phi(M) = \frac{1}{\Delta M} \sqrt{\sum_{i=1}^{N} \left(\frac{1}{C(M_i, z_i) V_{\rm max,i}} \right)^2}, \tag{2}$$

(Adams et al. 2023, 2024). We also account for the effect of cosmic variance. Since galaxy surveys sample the wider large-scale structure of the Universe, over/under-densities such as filaments and voids can bias measurements of the LF. We use the Trenti & Stiavelli (2008) calculator to estimate the uncertainty due to this effect. We find that cosmic variance contributes no more than 12% to the total error budget in our brightest bin, with Poissonian uncertainties dominating. We add these cosmic variance contributions in quadrature to the uncertainties calculated with Eq. (2). When computing the LF, we truncate to only include galaxies with $M_{\rm UV} < -20.7$, corresponding to the 50% completeness limit for the upper end of our redshift bin (see Fig. 4), to ensure a

Table 4: The UV LF values at $z \simeq 7$.

	UltraVISTA-only		UltraVISTA+*Euclid*	
$M_{\rm UV}$ (mag)	$n_{\rm gal}$	ϕ (mag^{-1} Mpc^{-3})	$n_{\rm gal}$	ϕ (mag^{-1} Mpc^{-3})
−22.6	5	$(1.31 \pm 0.60) \times 10^{-6}$	0	$< 1.83 \times 10^{-6}$
−22.2	12	$(3.33 \pm 1.03) \times 10^{-6}$	3	$(2.13 \pm 1.28) \times 10^{-6}$
−21.9	13	$(7.34 \pm 2.18) \times 10^{-6}$	4	$(6.03 \pm 3.19) \times 10^{-6}$
−21.7	11	$(6.28 \pm 2.02) \times 10^{-6}$	6	$(9.12 \pm 4.01) \times 10^{-6}$
−21.5	26	$(1.57 \pm 0.35) \times 10^{-5}$	10	$(1.59 \pm 0.56) \times 10^{-5}$
−21.3	43	$(2.74 \pm 0.50) \times 10^{-5}$	19	$(3.23 \pm 0.88) \times 10^{-5}$
−21.1	58	$(4.13 \pm 0.68) \times 10^{-5}$	25	$(4.42 \pm 1.09) \times 10^{-5}$
−20.9	47	$(3.83 \pm 0.68) \times 10^{-5}$	27	$(5.84 \pm 1.42) \times 10^{-5}$

Notes. The first column shows the central absolute UV magnitude $M_{\rm UV}$ of the bin. We then show the number of galaxies $n_{\rm gal}$ and the UV LF value and uncertainty for two cases: firstly for the U-only sample, and secondly for the U+E. The brightest two bins centred at $M_{\rm UV} = -22.6$ and -22.2 have a width of $\Delta M_{\rm UV} = 0.4$, and the remaining bins have width $\Delta M_{\rm UV} = 0.2$. We present the $1\,\sigma$ upper limit for the U+E bin at $M_{\rm UV} = -22.6$ (Gehrels 1986).

robust and complete sample is used for the LF determination. We choose $M_{\rm UV}$ bins such that they span the magnitude range of the sample down to the 50% completeness limit. The brightest bins centred at $M_{\rm UV} = -22.6$ and -22.2 have widths $\Delta M_{\rm UV} = 0.4$ to ensure that at least five galaxies lie within them for the U-only sample. The remaining bins centred at $M_{\rm UV} = -21.9$ down to $M_{\rm UV} = -20.3$ have narrower widths of $\Delta M_{\rm UV} = 0.2$. This provides a finer binning than used for the HST results of F15 and B21, whilst keeping at least ten galaxies in these narrower bins, benefiting both the fitting and the comparison with other studies. We use the same binning scheme for the U+E sample to provide a direct comparison between the two samples. The UV LFs from the two selections (U-only and U+E) are presented in Fig. 5, and the LF values are presented in Table 4.

5.3. Improved LF measurement with Euclid

Comparing the two LFs computed with each sample in Fig. 5, it is immediately clear that the U-only LF points show some scatter, whereas when *Euclid* is included in the SED fitting, the points follow a smooth decline towards the bright end. This is due to the additional *Euclid* photometry providing a better characterisation of LBGs and low-redshift interlopers, and including *Euclid* also allows for a more straightforward removal of VISTA crosstalk artefacts. Additionally, the *Euclid* photometry better probes the deep molecular absorption features seen in UCD SEDs, which are largely inaccessible with only ground-based NIR filters. Therefore, it is also the case that the UCD removal step, namely removing objects with $\chi^2_{\rm UCD} < \chi^2_{\rm gal}$, performs better with *Euclid* photometry since the degeneracy between a UCD SED and a flat UV continuum is broken. Additionally, the LF value of the faintest U-only bin at $M_{\rm UV} = -20.9$ decreases compared to the value at $M_{\rm UV} = -21.1$ (although are consistent within the uncertainties). When objects are selected in VISTA $Y + J$, the faintest sources may only have their detection in one or two of these filters, since the VISTA H and K_s filters drop in depth rapidly (see Table 1). On the other hand, *Euclid* provides uniform depth across all its NIR filters, leading to detections of the UV continuum across $\lambda_{\rm obs} = 1$–$2.5\,\mu$m for the faintest sources, leading to their robust characterisation as high-redshift LBGs. Finally, there is some scatter in the $M_{\rm UV}$ determined with and without the *Euclid* imaging. We show the differences in $M_{\rm UV}$ in Fig. B.1. This leads to some objects lying in different bins after the inclusion of *Euclid* data, providing an additional source of scatter in the LF bins. As shown in Fig. 3, the inclusion of *Euclid* photometry can alter the slope of the UV continuum slope, which contributes to differences in $M_{\rm UV}$. We further discuss the improved SED fitting constraints *Euclid* provides in Sect. 6.1.

The $2\,\sigma$ upper limit provided for the $M_{\rm UV} = -22.6$ bin for the U+E sample (following Gehrels 1986) is consistent with the LF value for the U-only sample in this bin. However, we find that the sources from this brightest bin which overlap with the *Euclid* footprint have their photometric redshifts shifted to $z > 7.5$ when *Euclid* photometry is included.

5.4. Double-power law and Schechter function fitting

Numerous studies have shown that a DPL provides a better fit to the UV LF at $z \simeq 7$ than a Schechter function, due to an excess of bright galaxies at $L > L^*$ (Bowler et al. 2014; B17; Harikane et al. 2022, V23; Harikane et al. 2025). We also note that gravitational lensing may play an important role in shaping the bright end, particularly at $z \geq 10$ with *Euclid* (Mason et al. 2015). The DPL has the functional form

$$\phi(M) = \frac{\phi^*}{10^{0.4\,(\alpha+1)\,(M-M^*)} + 10^{0.4\,(\beta+1)\,(M-M^*)}}\,, \tag{3}$$

where ϕ^* is the normalisation, M^* is the characteristic magnitude, α is the faint-end slope, and β is the bright-end slope. We fit a DPL to our U+E sample, incorporating bright-end results from V23 and faint-end results from F15. These two studies are chosen because they carefully remove UCD interlopers, providing natural extensions of the sample in this work to the bright and faint end. The best-fit parameters are presented in Table 5, and the resulting LF is shown in Fig. 6. Our fit yields bright- and faint-end slopes $\beta = -4.63^{+0.34}_{-0.39}$, $\alpha = -2.10^{+0.21}_{-0.17}$, with the knee given by $M^* = -21.14^{+0.28}_{-0.25}$ and $\phi^* = 0.91^{+0.67}_{-0.38} \times 10^{-4}$ mag^{-1} Mpc^{-3}. By means of the deep degree-scale imaging used in this work, this is the first time ground-based imaging has robustly probed fainter than the knee of the UV LF at $z \geq 6$. The constraints provided by combining UltraVISTA and *Euclid* also enable reliable sampling around $-22 \leq M_{\rm UV} \leq -21$, crucial for measuring M^* and ϕ^*. We also fit a Schechter function of the form

$$\phi(M) = 0.4\,\ln(10)\,\phi^*\,10^{0.4\,(M-M^*)\,(\alpha+1)}\,\exp\left(10^{-0.4\,(M-M^*)}\right)\,. \tag{4}$$

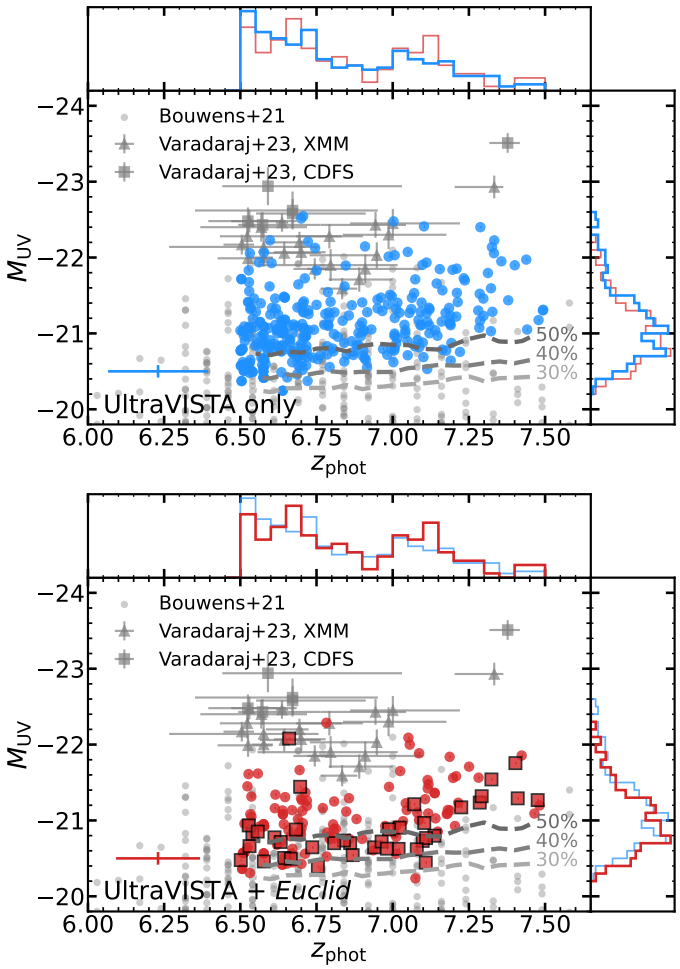

Fig. 4: The $z \simeq 7$ LBG sample from this work plotted in photometric redshift z_{phot} and absolute rest-frame UV magnitude M_{UV} space. *Top*: the U-only sample (blue). *Bottom*: the U+E sample (red). The red squares with a black outline indicate galaxies which are not recovered in the U-only sample, and are thus unique to the U+E sample. In both panels, we also show the candidates from V23 in the XMM-LSS and ECDF-S fields, and the HST-selected candidates from B21. The dashed grey lines show the 30%, 40%, and 50% completeness limits, as derived from the injection-recovery simulation (see Sect. 5.1). We also show the marginalised distributions in z_{phot} and M_{UV} as normalised histograms, and also overplot the distribution of the other sample as the thinner, fainter line for comparison. The mean uncertainties are shown on the bottom left.

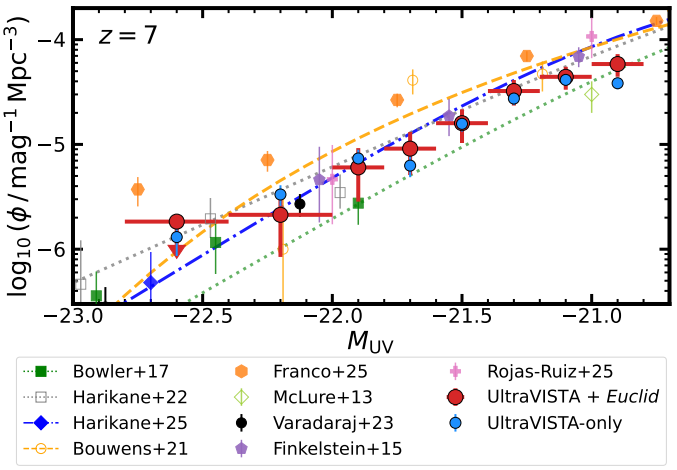

Fig. 5: A comparison of the UV LF at $z \simeq 7$ measured with the two samples presented in Fig. 4 and Sect. 4. The smaller blue circles show the LF points calculated from the U-only sample. The larger red circles show the LF points calculated from the U+E sample. We use the same binning in both cases, and the LF values are presented in Table 4. The brightest bin contains no galaxies from the U+E sample, so we show a $1\,\sigma$ upper limit whose value is noted in Table 4. We show results from McLure et al. (2013), F15, B17, B21 ($6.3 < z < 7.3$), Harikane et al. (2022, $6.3 < z < 7.7$), V23, Harikane et al. (2025), and Franco et al. (2025, $5.5 < z < 8.5$). Unless otherwise stated, these LFs are measured at $6.5 < z < 7.5$. Also shown are the best-fit Schechter and DPL fits found by B21 and Harikane et al. (2025) respectively.

The gradual decline seen in the LF points at $-22 < M_{UV} < -20.7$ is consistent with the Schechter function. In fact, the DPL and Schechter function are indistinguishable at $M_{UV} > -22.5$ However, at $M_{UV} < -22.5$, the Schechter function diverges from the best-fit DPL, and is unable to account for the brightest LF points of B17, V23, and Harikane et al. (2025).

Our derived slopes, α and β, are consistent with previous DPL measurements from B17 and Harikane et al. (2025) (see Fig. 8 for a comparison of the LF parameter measurements). The value of α also agrees with faint-end Schechter fits from F15 and B21. Our M^* is consistent with B17, Harikane et al. (2025), and the Schechter fit from F15, although note that the value of M^* derived from a Schechter fit by F15 is different from that for a DPL fit by the remaining studies. The value we derive for ϕ^* is also in agreement with these studies, but with smaller errors. Overall, our results agree with those of Harikane et al. (2025), who use a spectroscopically confirmed sample, eliminating contamination. This further suggests that we have effectively mitigated the encroachment of low-redshift interlopers into our $z \simeq 7$ U+E sample. Likewise, our DPL is consistent with B17, although with a slight shift to higher M^* and lower ϕ^*, but consistent within uncertainties. This implies that the constraining power of ground-based imaging for the LF, prior to sizeable overlap with space-based studies, was already quite strong. However, our results show that the gentle DPL decline continues down to the knee of the UV LF, providing a definitive measurement of the bright-end slope. This is best shown by the LF values of our faintest bins, which use deeper data and similar selection steps as B17, yet show no significant discrepancy with F15, indicating that there are no large systematic differences. The largest source of uncertainty in bright-end of the LF thus remains contamination by low-redshift interlopers and UCDs, reflected by relative excesses seen in Harikane et al. (2022, as discussed in V23) and B21. This is discussed further in the next section.

In the EAFs, *Euclid* will have substantial overlap with VIDEO. A selection similar to V23, but incorporating *Euclid* data to mitigate contamination, would be highly beneficial for confirming the bright-end shape. Additionally, future work in the EDFs utilising the DAWN survey (Euclid Collaboration: McPartland et al. 2025) will provide unprecedented constraints on the bright end with 53 deg^2 of imaging.

5.5. Comparison with other studies

In Fig. 5 we compare our LF points to other studies. Our results are consistent with the bright-end studies of B17, Harikane et al. (2022), V23, and Harikane et al. (2025), confirming a gradual decline in the LF at $M_{UV} < -22$. The constraining power of UltraVISTA DR6 is best seen at $M_{UV} > -22$. For this, we focus on the U+E results. As discussed in the previous section, our LF

Table 5: The best-fit parameters for the UV LF.

ϕ^* mag^{-1} Mpc^{-3}	M^* mag	α	β
$0.91^{+0.67}_{-0.38} \times 10^{-4}$	$-21.14^{+0.28}_{-0.25}$	$-2.10^{+0.21}_{-0.17}$	$-4.63^{+0.34}_{-0.39}$
$1.63^{+0.83}_{-0.61} \times 10^{-4}$	$-20.98^{+0.20}_{-0.21}$	$-1.98^{+0.18}_{-0.16}$	—

Notes. The parameters for the DPL fit are shown in the top row, and for the Schechter fit in the bottom row. We fit using our UV LF points, those from V23 and faint-end results from F15.

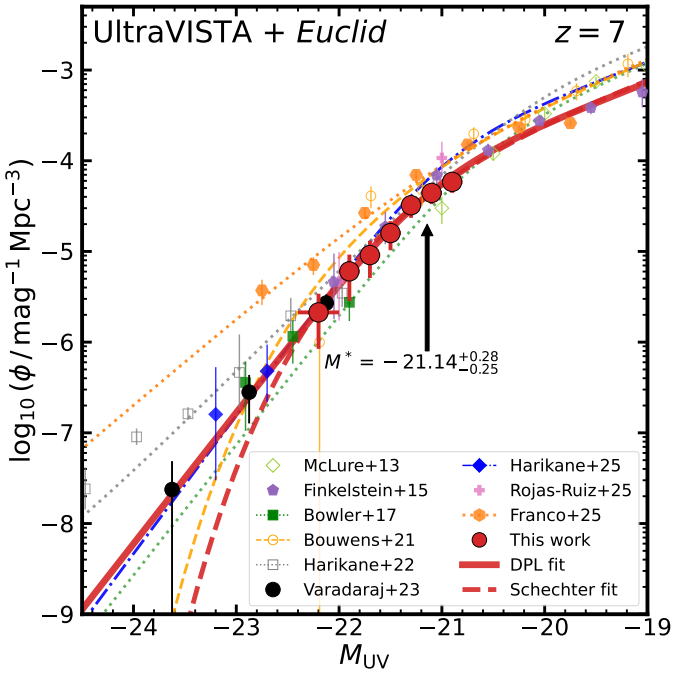

Fig. 6: The best-fit DPL and Schechter function for the UV LF at $z \simeq 7$, shown by the solid and dashed red lines, respectively. For the fitting we use results from this work (red points, the U+E sample), bright-end results from V23 (black points), and faint-end results from F15 (purple pentagons). We also show results at $6.5 < z < 7.5$ (unless otherwise stated) from McLure et al. (2013), F15, B17, B21 ($6.3 < z < 7.3$), Harikane et al. (2022) ($6.3 < z < 7.7$), Harikane et al. (2025), Franco et al. (2025) ($5.5 < z < 8.5$), and Rojas-Ruiz et al. (2025) ($7 < z \leq 8.4$). For comparison to our fit, we plot the best-fit DPLs from B17, Harikane et al. (2022), and Harikane et al. (2025).

points are remarkably consistent with the HST results of F15, indicating that any differences in methodology do not cause major systematic offsets. For example, UCD contaminants were removed by F15 using a combination of the `SExtractor` FWHM and their colours, whereas we use SED fitting. As we will show in Sect. 6.2, it is not possible to remove faint UCDs as being unresolved in the *Euclid* imaging at the magnitudes probed in this work. Additionally, F15 calculate the effective volume for a galaxy using their injection-recovery simulations, whereas we directly redshift the SED of each galaxy iteratively to determine its maximum redshift, and then its maximum occupied volume. In their simulations, they also allow the galaxy size to vary. F15 note that had they fixed their galaxy sizes to $R_e = 1$ kpc, they would have derived similar effective volumes, mirroring results from Grazian et al. (2012). F15 also determine their LF points using a non-parametric stepwise maximum likelihood calculation, although this approach produces equivalent results to the $1/V_{max}$ method for bins with high enough number counts. The consistency with F15, despite slight differing strategies for removing low-redshift interlopers, suggests that both of our approaches are successful at mitigating contamination.

Also, as discussed in the previous section, the consistency with the spectroscopic sample of Harikane et al. (2025) suggests little contamination in our sample. Similarly, we also find that our results are consistent with the findings of Rojas-Ruiz et al. (2025), who used the BoRG-JWST survey to spectroscopically confirm candidates identified in pure-parallel HST fields. In Fig. 5 we only compare to the sample from their GO 2426 program since it covers a similar redshift range, $7.0 < z \leq 8.4$, although extends to higher redshifts. However, there is little evolution in the bright end of the LF between $z = 7$–8 (V23).

Our four brightest U+E bins are in some tension with the brightest bins of B21, who see a drop of 1.6 dex between the two bins from $M_{UV} = -21.7$ to $M_{UV} = -22.2$. Since we are able to use narrower binning than the $\Delta M = 0.5$ mag bins used by B21 in this range, we can probe the finer evolution in number density across this magnitude range. We observe a gentle decline in the number density across our four brightest bins, dropping by only 0.9 dex, which is more consistent with the behaviour of the underlying DPL distribution of Harikane et al. (2025) compared to the Schechter function found by B21. Whilst the discovery of numerous $M_{UV} < -22.5$ galaxies at $z \simeq 7$ has convincingly ruled out the Schechter function form for the LF (Bowler et al. 2014; Harikane et al. 2022; V23), our results show this gradual decline also occurs from the knee of the LF. As discussed by F15 and B17, the discrepancy with B21 may be due to a lack of deep Y band imaging in the majority of the CANDELS fields, critical for determining the strength of a break to rule out UCDs and low-redshift galaxy interlopers.

Our LF values, when combined with V23, are significantly lower than the results of Franco et al. (2025) at $M_{UV} \leq -22$, who use the COSMOS2025 catalogue (Shuntov, Marko et al. 2025) to measure the UV LF in a redshift bin $z = 5.5$–8.5 from JWST COSMOS-Web imaging (Casey et al. 2023) by selecting sources which drop out of the HST F814W filter and are detected in JWST F115W (along with detections in the redder filters). For this sample they require F814W − F115W > 0.5, selecting the Lyman break. In this work, our reddest dropout filter, HSC i, is 0.8–1 mag deeper than our detection filters, Y and J. Additionally, I_E is 1.5 mag deeper than our detection filters. Franco et al. (2025) are likely robust against UCD contamination, since the high-resolution JWST imaging provides the means to remove them as point sources. However, the shallower depth of their dropout filter, relative to their detection filter, may introduce contamination by low-redshift dusty galaxies. A large magnitude difference between the dropout and detection filter is useful for distinguishing between a Balmer break and Lyman break. As discussed in V23, imposing a brighter selection in the detection filter provides one method for combatting a relatively shallow dropout filter.

5.6. Comparison with theory

In Fig. 7 we compare our UV LF results (along with results from V23) to predictions from various simulations and theoretical models. These include Delphi (Dayal et al. 2014, 2022), the Santa Cruz semi-analytical model (SAM, Yung et al. 2019), Astrid (Bird et al. 2022), DRAGONS (Liu et al. 2016), FLARES (Lovell et al. 2021; Vijayan et al. 2021; Wilkins et al. 2023), Thesan (Kannan et al. 2022), CoDa (Ocvirk et al. 2016), and DREaM (Drakos et al. 2022). We compare to these studies since they have a large enough volume to extend to at least $M_{UV} = -22$

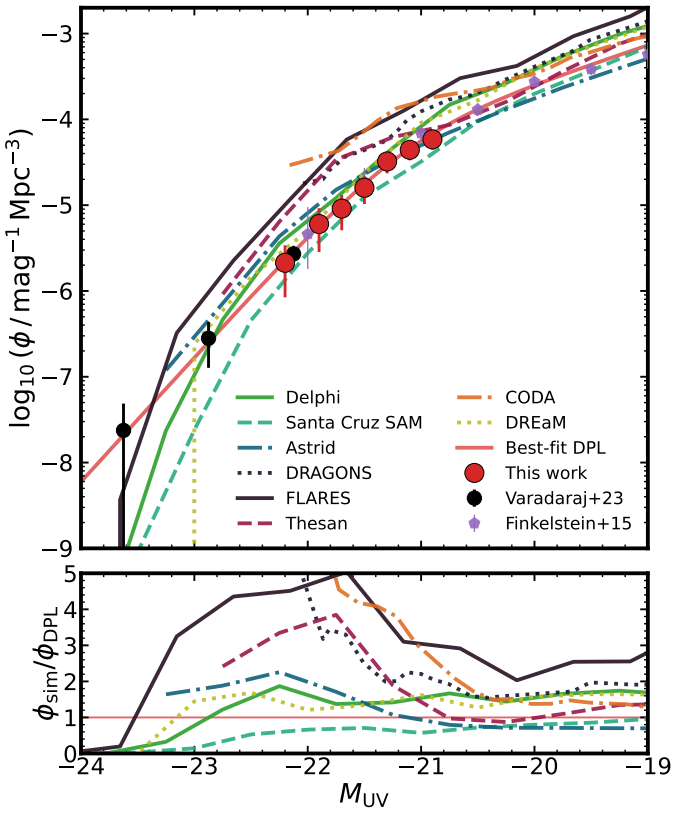

Fig. 7: A comparison of the UV LF measured in this work with predictions from semi-analytic models and hydrodynamic simulations. See section 5.6 for an outline of the studies. We also show LF results from V23 and F15. We show our best-fit DPL with the red line. The bottom panel shows the ratio of the LF predictions to our best-fit DPL, as a function of M_{UV}.

in their predictions of the UV LF at $z = 7$. Broadly speaking, there are two features that can be drawn from this comparison. Firstly, most of the predictions reproduce the faint end of the LF ($M_{\mathrm{UV}} \gtrsim -21$, although FLARES is in excess of our LF points by at least factor of two, and CoDa begins to over-predict significantly towards the knee of the LF). Secondly, it appears that there is a split in the bright end - some predictions are in significant excess of our results, whereas others agree with our results out to $M_{\mathrm{UV}} = -23$. Specifically, Delphi, Astrid and DREaM are consistent with our results. The Santa Cruz SAM is consistent out to $M_{\mathrm{UV}} = -22$, beyond which it begins to under-predict the LF. The agreement is likely because of the calibration of some of these simulations to relevant observations, in particular to observations of dust. For example, Delphi includes fully coupled treatment of metal and dust enrichment in order to explain the dust masses of REBELS galaxies (Bouwens et al. 2022; Inami et al. 2022), which are luminous LBGs at $z = 7$ selected from ground-based imaging, analogous to (and overlaps with) the sample presented in this work. The Santa Cruz SAM tunes the dust extinction optical depth to match the UV LF at $z = 4$–10. Astrid calibrates dust extinction at $z = 4$, and assumes no evolution of dust extinction across $z = 3$–10. DREaM calibrates its M_{UV}-stellar mass relation on results at $z \leq 4$, and extrapolations at $z > 4$ are consistent with observational results from Stark et al. (2013). On the other hand, DRAGONS and FLARES both calibrate their dust extinction on results from (Bouwens et al. 2014, 2015), which seems to cause a large excess compared to our results at $M_{\mathrm{UV}} = -22$. Both Thesan and CoDa discuss they do not produce enough dust in the highest mass haloes and at $M_{\mathrm{UV}} < -21$ respectively, explaining the excess.

Clearly, the shape of the bright end is highly sensitive to dust obscuration, and the prescription of dust is sensitive to the observations used to tune it. However, most predictions agree that significant reduction and steepening of the intrinsic UV LF occurs due to dust obscuration, producing the observed bright-end slope of $\beta \sim 4.5$–4.6, and galaxies at $z = 7$ with $M_{\mathrm{UV}} < -22$ are able to experience dust attenuation of up to 2 mag in the rest-frame UV. A suggestion by Dayal et al. (2022) is that the dust and star-forming regions are spatially offset, or perhaps a significant fraction of the total dust mass diffuses into the ISM, therefore no longer contributing to the attenuation of UV light. Indeed, recent studies have found significant dust build-up and offsets between dust and UV emission in $z \simeq 7$ LBGs (e.g. Bowler et al. 2022; Inami et al. 2022; Lines et al. 2025; Algera et al. 2026). There is still uncertainty in the $z = 7$ UV LF beyond $M_{\mathrm{UV}} < -23$, so pinning down the precise shape of the ultra-bright end with *Euclid* in the EDFs, whilst simultaneously making attempts to measure the dust content of the sample (akin to Bouwens et al. 2022) is critical for further comparison with simulations.

5.7. Comparison with JWST: a gradual evolution in the bright-end slope?

JWST has revolutionised our understanding of the $z > 7$ Universe by discovering luminous sources at early cosmic time (e.g. Naidu et al. 2022; Finkelstein et al. 2022; Castellano et al. 2022). However, ground-based imaging is still highly important for probing the bright-end of the LF at $z > 6$. Currently, JWST lacks the volume to probe the bright end. Additionally, at $z = 6$–7, without deep ancillary optical HST imaging, JWST does not have enough dropout filters bluewards of the expected position of the Lyman break at $\lambda_{\mathrm{obs}} \sim 1\,\mu$m. We also note that the luminous sources discovered by JWST are fainter than the brightest ground-based candidates presented in this work and in V23 (GNz-11 is currently the brightest spectroscopically confirmed galaxy at $z > 10$ with $M_{\mathrm{UV}} = -21.5$, Bunker et al. 2023). Our $z \simeq 7$ LBGs may be linked to these early sources. It is likely that $M_{\mathrm{UV}} < -22$ sources abundant in ground-based imaging at $z = 7$ occupy similar dark matter haloes to that of the brightest JWST sources such as JADES-GS-z14-0 and JADES-GS-z14-1 (Carniani et al. 2024), GHZ2 (Castellano et al. 2024), and GNz-11 (Bunker et al. 2023). It is thus natural to compare our LF results to $z > 7$ JWST results to understand the evolution of luminous LBGs in the first Gyr of cosmic time.

In Fig. 8 we show the evolution of the LF parameters across $z = 6$–13 from a range of ground-based, HST and JWST studies. We only show results from DPL fitting, and for β we only show results which have at least two LF points at $M_{\mathrm{UV}} < M^*$, such that they sufficiently probe the bright end. Note that JWST bright-end determinations have large error bars at $z > 9$ due to the limited volume available. We fit straight lines to these studies at $z \geq 6$ to probe the linear evolution, and find that, relative to $z = 6$, these can be expressed as

$$\begin{aligned}
\log_{10}(\phi^*/\,\mathrm{mag}^{-1}\,\mathrm{Mpc}^{-3}) &= (-3.40 \pm 0.15) \\
&\quad +(-0.17 \pm 0.05)\,(z-6)\,, \\
M^* &= (-20.99 \pm 0.15) + (0.19 \pm 0.07)\,(z-6)\,, \\
\alpha &= (-2.02 \pm 0.09) + (-0.08 \pm 0.05)\,(z-6)\,, \\
\beta &= (-4.91 \pm 0.29) + (0.39 \pm 0.13)\,(z-6)\,,
\end{aligned} \tag{5}$$

for the DPL LF parameters. Overall, our results are consistent with an evolution in the LF driven by a shallower β at higher

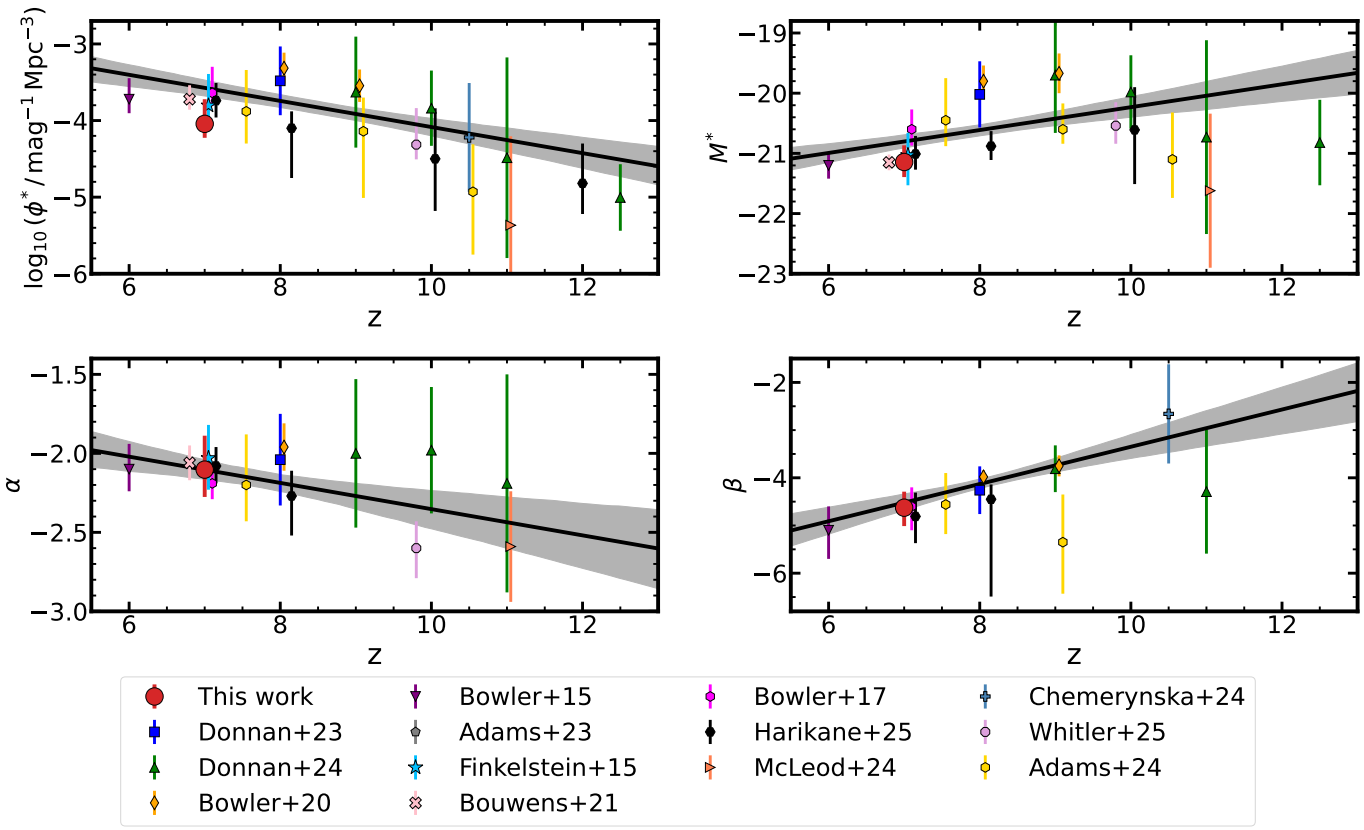

Fig. 8: The evolution of the DPL parameters with redshift, namely the normalisation ϕ^*, the characteristic magnitude M^*, the faint-end slope α, and the bright-end slope β (see Eq. 3). The red points show the parameters derived from DPL fitting in this work. We show a compilation of results at z = 6–12.5 from Bowler et al. (2015, 2020), B17, Adams et al. (2023, 2024), Donnan et al. (2023, 2024), Chemerynska et al. (2024), McLeod et al. (2024), Harikane et al. (2025), and Whitler et al. (2025) with some slight offsets in redshift for clarity. We do not show points from these studies which were fixed during the DPL fitting. For β, we only show studies which have at least two LF points brighter than their M^*, meaning they have some constraints on the bright-end slope. The black line indicates the best-fit straight-line to the $z \geq 6$ data. We also show the results of Schechter fitting from F15 and B21 for ease of comparison in Section 5.4.

redshifts, a mild evolution in the position of the knee, ϕ^* and M^*, and weak evolution in α. These results differ slightly from those of Bowler et al. (2020), who found that the evolution of the LF was dominated by β and M^*, with ϕ^* remaining relatively constant over z = 7–10. Donnan et al. (2024) use JWST multi-field imaging to show that ϕ^* has a stronger evolution than M^*, although they are required to fix their M^* at some redshifts. However, their evolution in ϕ^* is consistent with the luminous sources found at $z > 7$, with a gentle evolution in M^* allowing for the existence of these sources.

We note that a major caveat is that the LF parameters are degenerate during the fitting, limiting discussion regarding the evolution of ϕ^* and M^*. However, ground-based studies are able to probe sufficiently bright to determine the bright-end slope and allow for a meaningful discussion of the bright-end evolution. When fitting the evolution of β, we again note that we only used JWST studies that had at least two LF bins brightwards of their M^*, such that they sufficiently probe the bright-end of the LF. Comparing to the number of studies in the plot above for M^*, most JWST studies do not have the dynamic range to provide reliable measurements of the bright-end of the LF at $z > 8$, because large areas are needed to find the rarest sources. This is reflected in much smaller uncertainties on β from ground-based studies (Bowler et al. 2015; B17; Bowler et al. 2020; Donnan et al. 2023, and this work). A lack of bright-end measurements also results in weaker constraints on the knee of the LF. This can be seen in the large amounts of scatter in the values of M^* found by JWST studies. In fact, the increasing trend we see towards higher redshift is driven by the small uncertainties (relative to the JWST studies) on M^* found by the ground-based study of Bowler et al. (2020). Their small errors are caused by their sample lying entirely at $M_{\mathrm{UV}} < M^*$ (with DPL fits determined by combining with faint-end results from McLure et al. 2013 and McLeod et al. 2016). It is therefore not entirely clear whether M^* increases at higher redshift (as suggested by ground-based studies) or remains fairly constant with redshift (as suggested by JWST studies, but with large uncertainty). This demands a determination of the UV LF with *Euclid* at $z \geq 8$.

The DPL form of the LF at $z \simeq 7$ is more akin to the functional form of the halo mass function than a Schechter function, indicating that quenching of star formation and/or dust obscuration has not begun to dominate luminous LBGs at this epoch (Bowler et al. 2014). However, numerous studies have also shown that $z \simeq 7$ LBGs can host large dust reservoirs and exhibit signs of substantial dust obscuration (e.g. Bowler et al. 2024; Algera et al. 2026). The discrepancy arises due to unobscured star formation being probed by optical+NIR studies such as this work, and obscured star formation requiring submillimetre observations to measure the dust emission. Interestingly, we observe a gradual steepening in β from z = 9 down to z = 6 based on ground-based studies. The results of Chemerynska et al. (2024) and Donnan et al. (2024) are consistent with this

gradual evolution in β, but with larger uncertainties. Note that Chemerynska et al. (2024) use a large redshift bin of $9 < z < 12$, a useful strategy for boosting number counts over a redshift range corresponding to only 180 Myr. The bright-end slope is sensitive to dust obscuration (e.g. Cai et al. 2014) and quenching of star formation (Peng et al. 2010), so a gradual steepening at these epochs suggests a steady and gradual physical mechanism driving the evolution. Donnan et al. (2025) find tentative evidence that at fixed stellar mass, dust attenuation increases with decreasing redshift, in line with our steepening of β. We stress that *Euclid* studies are necessary to complement JWST for constraining the bright-end of the UV LF at $z \simeq 8$–10, which will reduce the roughly two magnitudes of scatter in M^* at these redshifts. *Euclid* studies will do this by identifying thousands of $M_{\rm UV} < -22$ sources in 53 deg^2 of imaging in the EDFs to depths comparable to UltraVISTA. However, based on the results of this work, it may be difficult to decontaminate UCDs from LFs determined from *Euclid* without some correction factors, due to the lack of ancillary NIR data available. Indeed, EDF-North is expected to have severe contamination due to a lower area of coverage by *Spitzer*/IRAC, and since this field is closer to the Galactic plane (Allen et al. in prep.).

6. Outlook for *Euclid*

In this section we explore the additional information provided by *Euclid* for our sample of $z \simeq 7$ LBGs, in terms of photometry and morphology.

6.1. SED fitting with Euclid

In Sect. 5 we have shown that adding *Euclid* photometry to SED fitting of our UltraVISTA-selected sample eliminates scatter in the LF points due to contamination and loss of genuine high-redshift galaxies. In Sect. 4 we have shown that *Euclid* recovers faint galaxies that are removed in the U-only selection. In this section we explore in further detail the additional information provided by the *Euclid* photometry with some example SED fits.

Returning to Fig. 3, where we show the SED fitting of a candidate LBG, LBG 10004+02015, we see that the *Euclid* photometry is powerful for identifying flat UV continuum slopes, and the deep $I_{\rm E}$ imaging strongly rules out low-redshift galaxy and M-type dwarf solutions, which do not exhibit as strong a break as LBGs. Although beyond the scope of this work, combined VISTA+*Euclid* photometry will be powerful for UV slope measurements. In this case, the addition of *Euclid* suggests a bluer UV slope than for the SED found with UltraVISTA NIR data alone. Note that the VISTA filters have shallower depths at longer wavelengths (see Fig. 1 and Table 1). The *Euclid* NISP filters have uniform depths, so the deep $H_{\rm E}$ imaging can allow for the discovery of very blue galaxies which would be undetected in VISTA H and K_s.

In Fig. 9 we show the SED fitting and postage stamp cutouts of two candidate T-type UCDs – one bright with $m_{\rm AB} = 25$, and one faint with $m_{\rm AB} = 26$. We first note that the brighter UCD has a clear point source morphology, which would allow for its removal from a LBG sample as being a point source. Such a removal would require an additional completeness calculation to account for the potential removal of active galactic nuclei and compact star-forming galaxies but would aid in improving the purity of $z = 7$ samples. However, the visual morphology of the fainter source is more ambiguous, with noise spikes beginning to contribute to the shape of the object, giving it a 'fuzzier' morphology. We discuss the prospect of removing UCDs based on size further in Sect. 6.2. Now looking to the SEDs for both candidate UCDs, we can see the deep absorption features with *Euclid* which are inaccessible with VISTA alone. The SED fitting for the brighter source also benefits from the pre-existing HSC optical photometry being able to detect the more gentle blue slope relative to a Lyman break. Prior to *Euclid*, this gentle blue slope, combined with deviations from flat NIR photometry, was the main discriminant used to remove UCDs in ground-based data. However, for the fainter UCD, the blue slope is not visible. As a result, it is more challenging to extend LBG searches down to the signal-to-noise limit without *Euclid*. This was a challenge encountered in V23 in the ECDF-S field due to a lack of deep optical imaging, where we selected objects in $Y+J$ at a brighter $8\,\sigma$ significance to account for this (compared to $5\,\sigma$ in this work), resulting in only six luminous galaxy candidates. VISTA imaging is available in the EAFs and in EDF Fornax as part of VIDEO imaging in ECDF-S. This overlap will be powerful for providing additional photometry on $z \geq 7$ sources found in ground-based imaging (e.g. Stefanon et al. 2019; Bowler et al. 2020; Donnan et al. 2023), as well as identifying new ones. A clear next step is to repeat this experiment with VISTA J- and H-band dropouts, and then adding in the *Euclid* photometry.

A natural experiment to conduct with the U+E sample is to test what fraction of these sources are recovered as high-redshift LBGs when only using *Euclid* photometry, i.e. when we remove the VISTA photometry (hereafter called E-only). Euclid Collaboration: van Mierlo et al. (2022) used real UltraVISTA galaxies at $z = 1$–8 and simulated *Euclid* photometry to predict the recoverability of UltraVISTA galaxies with *Euclid*. They found that 91 % of bright galaxies at $z > 6$ are recoverable, with a contamination rate of 20–40 % depending on magnitude. We repeated the SED fitting on the 108 galaxies in the U+E sample which are also present in the U-only sample. We recover 96 % of the sources with an E-only photometric redshift $z > 6$, and we recover 87 % with $|z_{\rm E-only} - z_{\rm U+E}| / (1 + z_{\rm U+E}) < 0.15$, consistent with the findings of Euclid Collaboration: van Mierlo et al. (2022). The $z_{\rm E-only}$ span from $z = 6$–8.3 since the wide *Euclid* filters are unable to precisely constrain the position of the Lyman break. An analysis of the contamination rate would require a reselection based on the *Euclid* imaging, which is beyond the scope of this work.

6.2. Can ultra-cool dwarfs be removed as point sources with Euclid?

It may be expected that space-based imaging with *Euclid* will allow for the removal of UCDs from LBG samples as unresolved sources. The first results from the Early Release Observations (EROs) were based on data that had a pixel scale of $0\farcs3\,{\rm pix}^{-1}$, which is larger than ground-based surveys such as VIDEO ($0\farcs2\,{\rm pix}^{-1}$, Jarvis et al. 2013). This allowed for the identification of $I_{\rm E}$ dropout sources as $z > 6$ LBG candidates, but objects were generally undersampled (Atek et al. 2025; Weaver et al. 2025). Weaver et al. (2025) injected PSF, clumpy, and disc models into the imaging and found that galaxies and PSFs are indistinguishable at this pixel scale, so no attempt was made to separate bright sources based on morphology.

We use `SExtractor` FWHMs to conduct a first-order analysis of LBG and UCD sizes in the *Euclid* PV imaging. This is possible thanks to the higher resolution of the *Euclid* imaging ($0\farcs1\,{\rm pix}^{-1}$ compared to $0\farcs15\,{\rm pix}^{-1}$ for UltraVISTA, with a PSF FWHM of $0\farcs5$ in NISP compared to $0\farcs85$ in VISTA Y). We first investigate the sizes of PSFs in the *Euclid* imaging. We take point sources from the JWST COSMOS-Web survey (Casey

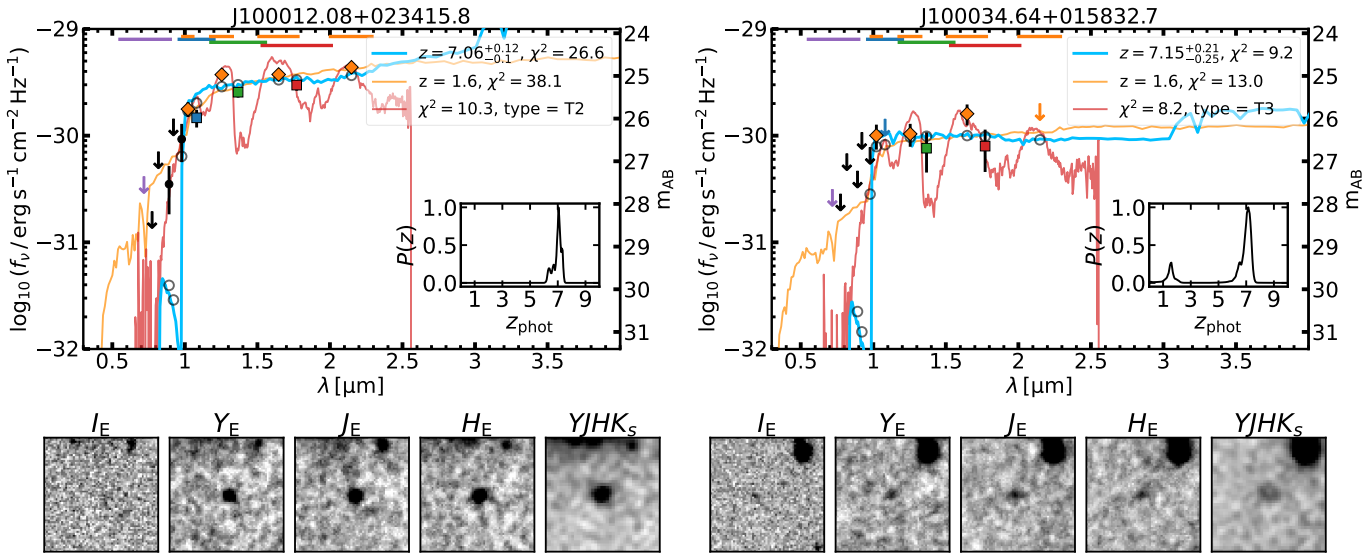

Fig. 9: SED fitting and postage stamp cutouts (in *Euclid* and a VISTA $YJHK_s$ stack) of two candidate T-type UCDs. *Left*: a brighter UCD with $m_{\rm AB} = 25$. *Right*: a fainter UCD with $m_{\rm AB} = 26$. As in Fig. 3, the orange diamonds represent the UltraVISTA photometry. The coloured squares show the *Euclid* photometry, with the $I_{\rm E}$ non-detection replaced with a $2\,\sigma$ upper limit. The remaining HSC photometry is shown by the black points. The coloured horizontal lines indicate the *Euclid* ad VISTA filter widths. The blue, orange, and red curves represent the high-redshift LBG, low-redshift dusty galaxy, and UCD solutions, respectively. The postage stamp cutouts are $6'' \times 6''$ and are scaled to saturate at $2\,\sigma$ below and $5\,\sigma$ above the noise level. Note the clear molecular absorption features seen by the VISTA+*Euclid* NIR photometry at $\lambda > 1$ μm. Also note the PSF-like morphology for the bright source, but a more irregular morphology for the faint source driven by noise.

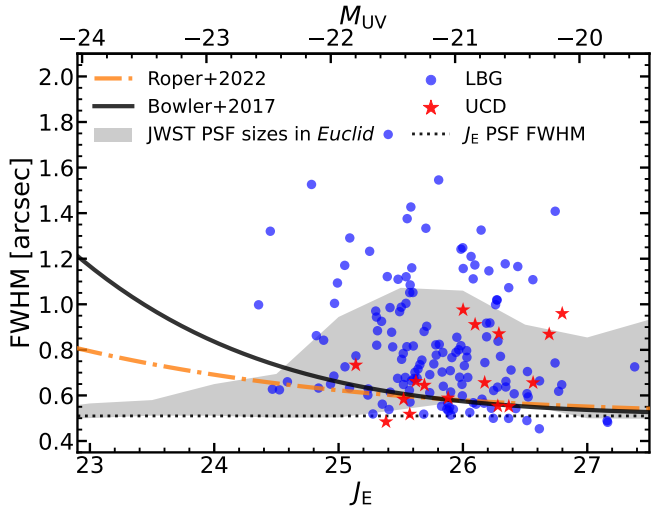

Fig. 10: The *Euclid* $J_{\rm E}$ FWHMs for sources identified as LBGs (blue dots) and UCDs (red stars) using SED fitting on HSC+VISTA+*Euclid* photometry. Also shown is the size-luminosity relation from HST imaging of a bright ground-selected sample (B17), and the prediction from the FLARES simulation (Roper et al. 2022). The dotted grey line is the median *Euclid* PSF FWHM. The grey shaded region shows the FWHMs of PSFs selected from JWST F444W imaging when they are observed in *Euclid* $J_{\rm E}$.

et al. 2023)[3], selected from the F444W FWHM-MAG_AUTO diagram using a catalogue produced with `SExtractor`. We then crossmatch these point sources with *Euclid*. F444W is thus used to provide the 'ground-truth', since the objects are unambiguously PSFs. Since F444W is much deeper than $J_{\rm E}$ ($5\,\sigma$ depth of 26.9 following the methodology in Sect. 2.5), we are able to select these 'ground-truth' PSFs far below the limiting magnitude of the *Euclid* imaging. In Fig. 10, the grey region show the `SExtractor` FWHM in *Euclid* $J_{\rm E}$ imaging of these JWST PSFs as a function of their $J_{\rm E}$ magnitude. This region is determined as the interquartile range around the median in magnitude bins of width 0.5 mag. For very bright ($J_{\rm E} \lesssim 24$) sources, PSFs in *Euclid* are consistent with the FWHM measured in Sect. 2.4, as expected. However, as we approach fainter magnitudes, the mean and standard deviation both begin to increase, before turning over near the limiting magnitude of the $J_{\rm E}$ imaging. This behaviour is expected as noise begins to boost the FWHM measurements of faint sources. Additionally, the turnover is caused by biases in the selection of faint PSFs in the *Euclid* imaging, since only those with an associated large positive noise will be detected. Bowler et al. (2014) conduct a similar investigation by injecting PSFs into UltraVISTA and UDS imaging, and find similar behaviour. In Fig. 10 we also show the FWHM-$J_{\rm E}$ magnitude distribution of LBGs and UCDs identified through SED fitting with combined HSC+VISTA+*Euclid* photometry for the U+E sample. The FWHMs of the UCDs are consistent with the shaded region. Additionally, none of the UCDs identified with SED fitting exceed a FWHM of 1″. Whilst a large fraction of the LBG sample has FWHMs above 1″, the majority are consistent with the scatter in sizes measured for point sources. Some LBGs have FWHMs consistent with that of the PSF. These could be compact sources with high star-formation surface densities (Morishita et al. 2024; Harikane et al. 2025). We also show the size-luminosity relations determined by B17 from HST imaging of a ground-based sample, and the prediction from the FLARES simulation (Roper et al. 2022). The size-luminosity relation can be written as

$$R_{\rm e} = R_0 \left(\frac{L}{L_0} \right)^{\gamma} , \tag{6}$$

[3] The data described here may be obtained from https://doi.org/10.17909/g3fb-ez59.

where L_0 is the characteristic luminosity corresponding to an absolute magnitude $M = -21$, R_0 is the size at L_0 and γ is the slope of the relation. We convert their relations for the effective radius in terms of R_e in kpc to an FWHM by assuming the galaxies have a Sérsic profile with index $n = 1$, corresponding to an exponential disc. Results from JWST show that galaxies at $z \simeq 7$ are well-fit by such profiles (e.g. Kartaltepe et al. 2023; Ormerod et al. 2024; Westcott et al. 2025). We then convolve the literature size-luminosity relations with the *Euclid* PSF in order to simulate what would be seen with *Euclid* in terms of FWHM. For this, we follow Oesch et al. (2010) and add the measured PSF size in quadrature. We note that the UV size-luminosity relation at $z = 7$ has been measured by HST and JWST (e.g. Shibuya et al. 2015; Yang et al. 2022, respectively). However, due to the lack of area, these studies do not place strong constraints on the very bright end. Yang et al. (2022) base their results on lensed galaxies to place constraints on the ultra-faint end of this relation, but only have one source with $M_{\rm UV} < -22$ at $z = 6$–7. Shibuya et al. (2015) is based on a brighter sample, but only have two sources with $M_{\rm UV} < -22$ at $z \simeq 7$ (see their figure 9). The relation determined by B17 is currently the only relation at $z = 7$ which samples galaxies at $M_{\rm UV} < -22$ (with HST follow-up of ground-selected LBGs), once again highlighting the necessity for ground-selected samples prior to *Euclid*. They find a size-luminosity relation with slope $\gamma = 0.50$. This provides a positive forecast for the removal of UCDs as PSFs as point sources, since it suggests that galaxies will grow rapidly in size at $M_{\rm UV} < -22$. As shown in Fig. 10, the FWHMs of JWST PSFs, as measured from *Euclid* $J_{\rm E}$ imaging, deviates from the B17 size-luminosity relation at $J_{\rm E} \lesssim 24.5$. The prediction from the FLARES simulation (Roper et al. 2022) also shows a similar deviation in the size-magnitude relation from the point source sizes at bright magnitudes. Comparison to these studies suggests that within the EDFs at these magnitudes, where VISTA imaging is not available to remove UCDs with SED fitting, it will be possible to remove UCDs as unresolved sources in bright samples (noting expected $5\,\sigma$ depths in the EDFs of around 26).

The key VISTA fields (COSMOS for UltraVISTA, XMM-LSS and ECDF-S for VIDEO) cover around $10\,{\rm deg}^2$ and will overlap with both the *Euclid* Deep/Auxiliary Fields, also expected to reach depths of 26. This offers the unique opportunity to identify LBGs and UCDs with SED fitting and determine a size-luminosity relation for the most luminous $z \simeq 7$ LBGs. Additionally, at $z \simeq 6$ and below, the UV continuum will enter $I_{\rm E}$, which has a much smaller PSF FWHM than NISP. *Euclid* will thus provide some of first resolved measurements of ultra-luminous sources in the middle of, towards the end of, and after reionisation.

6.3. Lessons learned for the Euclid Deep Fields

Our results have shown that additional ground-based NIR photometry is powerful for removing L- and T-type UCDs via SED fitting, which *Euclid* alone is unable to do due to its broad filter response curves (see Fig. 1). We have also shown that in the range $25 < J < 27$, UCDs cannot be cleanly removed from an LBG sample as point sources because noise spikes contribute to the morphology of faint point sources, and the size-luminosity relation of LBGs corresponds to a small FWHM. This is critical for the EDFs because they will eventually reach $5\,\sigma$ depths of around 26, allowing for the discovery of many sources in this magnitude range. At $J \lesssim 24.5$, this will be much easier since UCDs will have a clear PSF morphology and LBGs are expected to be larger (B17). At these redshifts, however, Little Red Dots (Matthee et al. 2024) may also exhibit a clear PSF morphology. These are sources with a distinct V-shaped SED, compact morphology and a large subset of these have broad Hα lines, indicating that they may harbour supermassive black holes (e.g. Harikane et al. 2023b; Greene et al. 2024; Kocevski et al. 2025). Additionally, at these magnitudes, one may expect to also find quasars which will have a PSF morphology. It may be possible to distinguish these from UCDs based on the strength of the $I_{\rm E} - Y_{\rm E}$ break at $z > 6$ (Euclid Collaboration: Barnett et al. 2019), although this is expected to be quite difficult (Bañados et al. 2025). Full SED fitting and Bayesian classification methods are likely required to identify quasars and Little Red Dots, along with spectroscopic follow-up. Despite this, bright magnitudes ($J \lesssim 24.5$) are the strength of the EDFs, where there will be enough area to discover many of these rare, ultra-luminous LBGs. However, the EDFs will not have ancillary NIR data to help remove UCDs via SED fitting – although Rubin/LSST will provide imaging in EDF-Fornax and EDF-South in the optical *ugrizy* filters in the southern sky, allowing for the UCD blue-end slope to be detected (see Fig. 9). This means relatively faint samples at $J > 25$ may still suffer from contamination by UCDs. This magnitude range is, however, the strength of the key VISTA fields, namely XMM-LSS, ECDF-S and COSMOS, where VISTA surveys such as VIDEO and UltraVISTA have/will have overlap with *Euclid* imaging. We suggest that $z \gtrsim 7$ LBG searches in the EDFs should focus on bright selections at $J < 25$ to mitigate contamination, and supplement this with selections in the VISTA fields where SED fitting can be used to construct clean samples. There is the potential to use ancillary *Spitzer*/IRAC to reduce contamination rates. However, at $J > 25$, the available *Spitzer*/IRAC imaging would be too shallow, as found for the faint end of the sample in this work, further motivating a selection at $J < 25$.

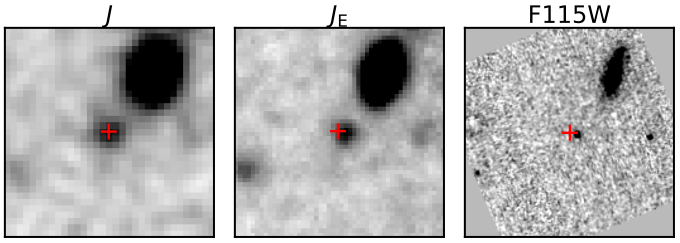

Fig. 11: Proper motion of a candidate UCD. The postage stamp cutouts show the source in VISTA J, $J_{\rm E}$, and F115W from JWST. The cutouts are $5'' \times 5''$ and saturate at $2\,\sigma$ and $5\,\sigma$ below and above the noise level. The red crosshair is placed at the centroid of the source as determined from the VISTA image to highlight the proper motion when observed with *Euclid* and JWST.

Not only is SED fitting powerful in these fields, but since *Euclid* imaging has been taken over a decade after the beginning of VIDEO and UltraVISTA, some of the brightest candidate UCDs found in our selection show small amounts of proper motion. In Fig. 11 we show an example, with the offset relative to VISTA being much clearer when compared to imaging from JWST COSMOS-Web. We note this source is removed from the sample based on SED fitting. However, sources with large proper motion are removed as part of our selection, since they will have a low or non-detection in *Euclid*, resulting in a poor SED fit. Additionally, we do not use proper motion as a screening step since this is complicated by the appearance of faint stars in *Euclid*, as discussed in Sect. 6.2. Removal of UCDs by their proper motion will be thus be more viable in the EDFs.

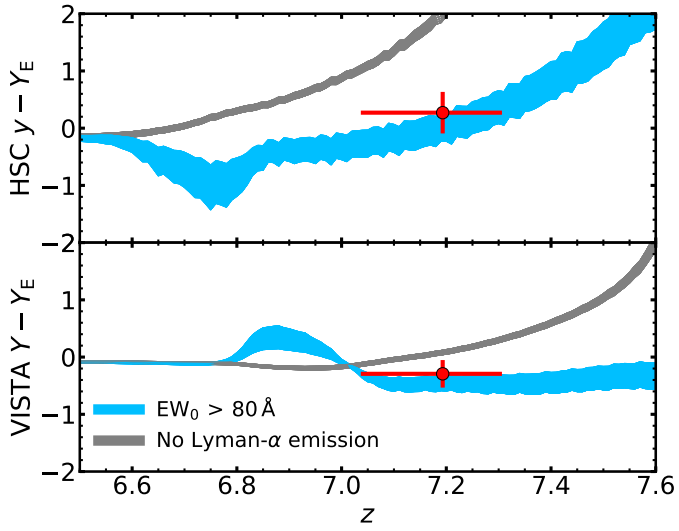

Fig. 12: The expected HSC $y - Y_E$ (*top*) and VISTA $Y - Y_E$ colours (*bottom*) of LBGs (grey) and strong ($\mathrm{EW_0} > 80$ Å) LAEs (blue) as a function of redshift, generated using mock BAGPIPES galaxies. The red point shows the position of our LAE candidate (see Fig. 13) in this colour-redshift space.

6.4. Lyman–α emitters with pseudo-narrowbands

Euclid not only provides strong colour information on L- and T-type dwarfs when combined with VISTA, but can also reveal the nature of LBGs with strong emission lines. The identification of emission lines with photometry has been done before using *Spitzer*/IRAC colours to identify strong [OIII]+Hβ emitters (e.g. Smit et al. 2015; Roberts-Borsani et al. 2016) which have then been found to be LAEs through spectroscopic follow-up (e.g. Oesch et al. 2015). Ground-based studies have used narrowbands to identify LAEs in narrow redshift ranges (e.g. Bañados et al. 2013; Endsley et al. 2021b; Umeda et al. 2025; Lambert et al. 2024), and JWST has used medium- and narrowbands to search for flux excess relative to the broadband photometry (e.g. JELS, Duncan et al. 2025; Pirie et al. 2025). The overlap of the HSC y, VISTA Y and *Euclid* Y_E filters around $\lambda = 1\,\mu$m (see Fig. 1) provides a unique opportunity to identify strong Lyman-α emitters, since the filters will behave differently as the line is redshifted through the filters relative to a normal Lyman-break. We use BAGPIPES (Carnall et al. 2018) to generate the synthetic galaxy photometry with $A_V = 0$–0.6, allowing ages up to the age of the Universe at a given redshift and subsolar metallicity $Z = 0.2\,Z_\odot$. Since BAGPIPES does not model Lyα emission, we add the line with equivalent widths $\mathrm{EW_0} = 80$–240 Å. This is done in the same manner as in Sect. 3.2, by measuring the continuum level between $\lambda_{\mathrm{rest}} = 1250$–$1300$ Å. In Fig. 12, we show the HSC $y - Y_E$ and VISTA $Y - Y_E$ colours of LBGs and LAEs with rest-frame equivalent width $\mathrm{EW_0} > 80$ Å. A strong colour difference can be seen between the LBGs and LAEs at $z > 7$. We find one source at $z = 7.19$ (EUCL J100028.39+021508.0) which lies within the LAE colour region. The SED fitting for this galaxy, along with postage stamp cutouts, is shown in Fig. 13. A clear excess in flux is seen in VISTA Y relative to HSC y and Y_E, boosted by a potential strong Lyα emission line. The morphology in VISTA Y also differs from Y_E with an additional clump to the north-east. Physical offsets between the UV continuum and Lyα emission are often seen in LAEs targeted by MUSE (e.g. Claeyssens et al. 2022), thought to be caused by star-forming substructures, merging galaxies or scattering effects inside the circumgalactic medium. Follow-up imaging with the F090W NIRCam filter would confirm the Lyman-α morphology. This source also overlaps with JWST COSMOS-Web, and these stamps are also shown in Fig. 13. We use BAGPIPES to conduct SED fitting using the additional JWST photometry to determine the physical properties of this galaxy. We fix the redshift to that found by LePhare, $z = 7.19$. We use a delayed-τ SFH and allow the time since star formation began to vary between 10 Myr and the age of the Universe at this redshift, and allow the characteristic timescale τ to vary between 50 Myr and 10 Gyr. We fix metallicity to $Z = 0.2\,Z_\odot$. We find that this galaxy has a mass of $\log_{10}(M_*/M_\odot) = 9.81^{+0.13}_{-0.20}$ and a star-formation rate of around $26\,M_\odot\,\mathrm{yr}^{-1}$. This source was previously identified in the COSMOS2020 Farmer catalogue (Weaver et al. 2022) as a $z = 7$ galaxy with Farmer ID 586756. Additionally, based on a continuum level of $\sim 1.3 \times 10^{-30}\,\mathrm{erg\,s^{-1}\,cm^{-2}\,Hz^{-1}}$ and an equivalent width $\mathrm{EW_0} = 240$ Å, we estimate a Lyα line flux of $7.7 \times 10^{-17}\,\mathrm{erg\,s^{-1}\,cm^{-2}\,Hz^{-1}}$ and a Lyα luminosity $L_{\mathrm{Ly}\alpha} = 5.5 \times 10^{43}\,\mathrm{erg\,s^{-1}}$.

This galaxy is an ideal candidate for follow-up observations with JWST and ALMA, since similar sources have shown signs of primordial ISM conditions, Lyα haloes, and complex gas exchange mechanisms between components, hinting at merging activity (e.g. 'Himiko' and 'COSMOS Redshift 7', see Ouchi et al. 2013; Sobral et al. 2015; Marconcini et al. 2025; Kiyota et al. 2025). Based on the estimated line flux, this source would also be detectable with ground-based observatories such as Keck (Schenker et al. 2012). Looking forward, the three filters used to identify this source will also be available in the XMM-LSS field as part of the EAFs and Euclid Wide Survey, providing additional opportunities to identify strong LAEs embedded in the Epoch of Reionisation. In the Euclid Wide Survey, overlap with the LSST y filter can also be used to identify such sources. LAEs at lower redshifts can be identified in the EDFs by comparing HSC r, i, and z to the *Euclid* I_E filter, although this will be more difficult due to overlap between only two filters at a time and the large width of I_E. Finally, the EDFs and EAFs will be observed with the blue and red grism (BG_E and RG_E) available with NISP-S, covering $\lambda = 0.9$–$1.9\,\mu$m (Euclid Collaboration: Jahnke et al. 2025; Euclid Collaboration: Mellier et al. 2025). Current observations with NISP-S in the EAFs are not deep enough to detect Lyman-α emission at $z = 7$, since the SIR pipeline only does spectral extraction with $H_E < 22.5$. However, in future data releases, this threshold is planned to be brought down to $H_E < 24$. BG_E will be able to detect Lyman-α emission at $z = 6.5$–10, providing a method for redshift confirmation of LAE candidates presented in this work, as well as a sample of extreme line emitters over degree scale imaging.

7. Summary

We have conducted a search for $z \simeq 7$ LBGs in the final data release (DR6) of the UltraVISTA survey, covering $1.72\,\mathrm{deg}^2$. We combine this NIR imaging with deep optical imaging from HSC and infrared imaging from *Spitzer*/IRAC to conduct a full SED fitting analysis using LePhare. We conduct two different selections: one where *Euclid* photometry is included for the SED fitting (the U+E sample), and one without the use of *Euclid* (the U-only sample). The U-only sample consists of 289 candidate galaxies at $6.5 \leq z_{\mathrm{phot}} \leq 7.5$ with $-22.5 \leq M_{\mathrm{UV}} \leq -20.2$. With the improved depth of UltraVISTA DR6, this sample reaches faint enough magnitudes to overlap with the HST-selected sam-

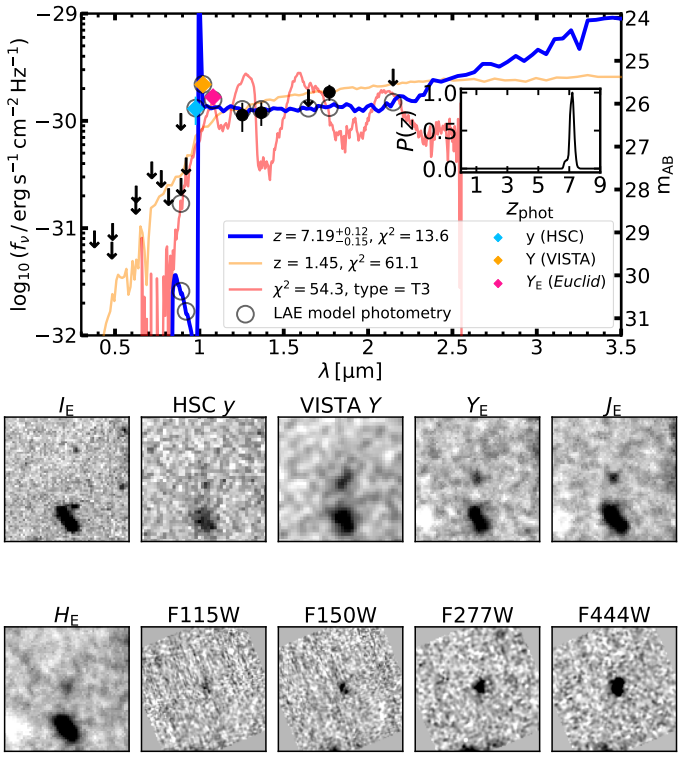

Fig. 13: SED fitting (*top*) and postage stamp cutouts (*bottom*) of our LAE candidate, EUCL J100028.39+021508.0. The SED fitting plot is similar to Fig. 3, but here we colour the HSC y, VISTA Y and *Euclid* Y_E filters differently to highlight them. The ground-based and *Euclid* stamps are 6″×6″ and the JWST stamps are 3″×3″. The stamps saturate at 2 σ below and 5 σ above noise level.

ples of F15 and B21. The U+E sample consists of 140 galaxies, with 38 not identified in the U-only sample. *Euclid* acts to recover very faint galaxies which lack robust SED constraints in VISTA photometry alone.

We find that *Euclid* comprehensively addresses contamination by UCDs and artefacts, as well as the unintended removal of genuine galaxy candidates, seen as scatter in the UV LF points computed from the U-only sample. Correspondingly, the UV LF based on the U+E sample shows a smooth decline in number density towards brighter magnitudes, in excellent agreement with F15 as well as previous bright-end studies (B17; V23; Harikane et al. 2025). Our DPL fitting reveals that this ground-selected sample probes fainter than the LF knee for the first time at $z > 6$. We compare our UV LF at $z \simeq 7$ to JWST results at $z > 7$. We find some evidence for a gentle evolution in the bright-end slope, although this is limited by a lack of robust measurements of the bright end at $z > 9$, which will require robust samples from current and upcoming degree-scale JWST programmes as well as the EDFs.

We then explore in detail the additional information provided by *Euclid* for this UltraVISTA-selected sample. We show that whilst combined VISTA+*Euclid* photometry is powerful for removing faint UCDs via SED fitting, at the magnitudes probed in this work UCDs cannot be separated morphologically from LBG samples as point sources. This is because faint point sources have their FWHMs boosted by positive noise spikes. At $J \lesssim 24.5$, since the size-luminosity relation of galaxies rapidly increases, we forecast that it will be straightforward to remove UCDs based on their morphology. This is particularly crucial for the EDFs where ancillary NIR data are lacking.

Finally, we also present an extreme Lyman-α emitter candidate at $z = 7.2$ identified via its strong colours in HSC $y - Y_E$ and VISTA $Y - Y_E$, differing significantly from the expected colours of a normal LBG. The differences in morphology between VISTA Y and Y_E may indicate a Lyα-emitting clump physically offset from the UV continuum. These three slightly different y filters will be available in XMM-LSS, providing further opportunity for the identification of extreme sources during the Epoch of Reionisation. Such sources are prime candidates for follow-up with JWST.

Data Availability

Table 3, which provides the photometry and properties of the U+E sample, along with a similar table for the U-only sample, and 10″ × 10″ postage stamp cutouts of the U+E sample in the *Euclid* I_E, Y_E, J_E, and H_E filters, are available in electronic form at the CDS via anonymous ftp to cdsarc.u-strasbg.fr (130.79.128.5) or via http://cdsweb.u-strasbg.fr/cgi-bin/qcat?J/A+A/.

Acknowledgements. RGV acknowledges funding from the Science and Technology Facilities Council (STFC; grant code ST/W507726/1). RAAB acknowledges support from an STFC Ernest Rutherford Fellowship (grant number ST/T003596/1). MJJ acknowledges support of the STFC consolidated grants (ST/S000488/1 and ST/W000903/1) and from a UKRI Frontiers Research Grant (EP/X026639/1). MJJ also acknowledges support from the Oxford Hintze Centre for Astrophysical Surveys that is funded through generous support from the Hintze Family Charitable Foundation. The Cosmic Dawn Center (DAWN) is funded by the Danish National Research Foundation under grant DNRF140. The Euclid Consortium acknowledges the European Space Agency and a number of agencies and institutes that have supported the development of *Euclid*, in particular the Agenzia Spaziale Italiana, the Austrian Forschungsförderungsgesellschaft funded through BMK, the Belgian Science Policy, the Canadian Euclid Consortium, the Deutsches Zentrum für Luft- und Raumfahrt, the DTU Space and the Niels Bohr Institute in Denmark, the French Centre National d'Etudes Spatiales, the Fundação para a Ciência e a Tecnologia, the Hungarian Academy of Sciences, the Ministerio de Ciencia, Innovación y Universidades, the National Aeronautics and Space Administration, the National Astronomical Observatory of Japan, the Netherlandse Onderzoekschool Voor Astronomie, the Norwegian Space Agency, the Research Council of Finland, the Romanian Space Agency, the State Secretariat for Education, Research, and Innovation (SERI) at the Swiss Space Office (SSO), and the United Kingdom Space Agency. A complete and detailed list is available on the *Euclid* web site (www.euclid-ec.org). This work is based on observations collected at the European Southern Observatory under ESO programmes 179.A-2005, 198.A-2003, 1104.A-0643, 110.25A2 and 284.A-5026 and on data obtained from the ESO Science Archive Facility with DOI https://doi. org/10.18727/archive/52, and on data products produced by CANDIDE and the Cambridge Astronomy Survey Unit on behalf of the UltraVISTA consortium. The Hyper Suprime-Cam (HSC) collaboration includes the astronomical communities of Japan and Taiwan, and Princeton University. The HSC instrumentation and software were developed by the National Astronomical Observatory of Japan (NAOJ), the Kavli Institute for the Physics and Mathematics of the Universe (Kavli IPMU), the University of Tokyo, the High Energy Accelerator Research Organization (KEK), the Academia Sinica Institute for Astronomy and Astrophysics in Taiwan (ASIAA), and Princeton University. Funding was contributed by the FIRST program from the Japanese Cabinet Office, the Ministry of Education, Culture, Sports, Science and Technology (MEXT), the Japan Society for the Promotion of Science (JSPS), Japan Science and Technology Agency (JST), the Toray Science Foundation, NAOJ, Kavli IPMU, KEK, ASIAA, and Princeton University. This paper is based on data collected at the Subaru Telescope and retrieved from the HSC data archive system, which is operated by the Subaru Telescope and Astronomy Data Center (ADC) at NAOJ. Data analysis was in part carried out with the cooperation of Center for Computational Astrophysics (CfCA), NAOJ. This work is based in part on observations made with the NASA/ESA/CSA James Webb Space Telescope. The data were obtained from the Mikulski Archive for Space Telescopes at the Space Telescope Science Institute, which is operated by the Association of Universities for Research in Astronomy, Inc., under NASA contract NAS 5-03127 for JWST. These observations are associated with program #1727.

References

Adamo, A., Atek, H., Bagley, M. B., et al. 2025, Nature Astronomy, 9, 1134

Adams, N. J., Bowler, R. A. A., Jarvis, M. J., et al. 2020, MNRAS, 494, 1771
Adams, N. J., Bowler, R. A. A., Jarvis, M. J., Varadaraj, R. G., & Häußler, B. 2023, MNRAS, 523, 327
Adams, N. J., Conselice, C. J., Austin, D., et al. 2024, ApJ, 965, 169
Aihara, H., AlSayyad, Y., Ando, M., et al. 2022, PASJ, 74, 247
Algera, H. S. B., Rowland, L., Stefanon, M., et al. 2026, MNRAS, 545, staf1897
Arnouts, S., Cristiani, S., Moscardini, L., et al. 1999, MNRAS, 310, 540
Ashby, M. L. N., Caputi, K. I., Cowley, W., et al. 2018, ApJS, 237, 39
Ashby, M. L. N., Willner, S. P., Fazio, G. G., et al. 2015, ApJS, 218, 33
Atek, H., Gavazzi, R., Weaver, J., et al. 2025, A&A, 697, A15
Bañados, E., Le Brun, V., Belladitta, S., et al. 2025, MNRAS, 542, 1088
Bañados, E., Venemans, B., Walter, F., et al. 2013, ApJ, 773, 178
Bailey, J., Simpson, A., & Crisp, D. 2007, PASP, 119, 228
Bertin, E. 2006, in Astronomical Society of the Pacific Conference Series, Vol. 351, Astronomical Data Analysis Software and Systems XV, ed. C. Gabriel, C. Arviset, D. Ponz, & S. Enrique, 112
Bertin, E. 2011, in Astronomical Society of the Pacific Conference Series, Vol. 442, Astronomical Data Analysis Software and Systems XX, ed. I. N. Evans, A. Accomazzi, D. J. Mink, & A. H. Rots, 435
Bertin, E. & Arnouts, S. 1996, A&AS, 117, 393
Bertin, E., Mellier, Y., Radovich, M., et al. 2002, in Astronomical Society of the Pacific Conference Series, Vol. 281, Astronomical Data Analysis Software and Systems XI, ed. D. A. Bohlender, D. Durand, & T. H. Handley, 228
Bird, S., Ni, Y., Di Matteo, T., et al. 2022, MNRAS, 512, 3703
Boucaud, A., Bocchio, M., Abergel, A., et al. 2016, A&A, 596, A63
Bouwens, R. J., Illingworth, G. D., Oesch, P. A., et al. 2014, ApJ, 793, 115
Bouwens, R. J., Illingworth, G. D., Oesch, P. A., et al. 2015, ApJ, 803, 34
Bouwens, R. J., Oesch, P. A., Stefanon, M., et al. 2021, AJ, 162, 47
Bouwens, R. J., Smit, R., Schouws, S., et al. 2022, ApJ, 931, 160
Bowler, R. A. A., Cullen, F., McLure, R. J., Dunlop, J. S., & Avison, A. 2022, MNRAS, 510, 5088
Bowler, R. A. A., Dunlop, J. S., McLure, R. J., et al. 2012, MNRAS, 426, 2772
Bowler, R. A. A., Dunlop, J. S., McLure, R. J., et al. 2015, MNRAS, 452, 1817
Bowler, R. A. A., Dunlop, J. S., McLure, R. J., & McLeod, D. J. 2017, MNRAS, 466, 3612
Bowler, R. A. A., Dunlop, J. S., McLure, R. J., et al. 2014, MNRAS, 440, 2810
Bowler, R. A. A., Inami, H., Sommovigo, L., et al. 2024, MNRAS, 527, 5808
Bowler, R. A. A., Jarvis, M. J., Dunlop, J. S., et al. 2020, MNRAS, 493, 2059
Bruzual, G. & Charlot, S. 2003, MNRAS, 344, 1000
Bunker, A. J., Saxena, A., Cameron, A. J., et al. 2023, A&A, 677, A88
Burgasser, A. J. 2014, in Astronomical Society of India Conference Series, Vol. 11, Astronomical Society of India Conference Series, 7–16
Burgasser, A. J., Bezanson, R., Labbe, I., et al. 2024, ApJ, 962, 177
Cai, Z.-Y., Lapi, A., Bressan, A., et al. 2014, ApJ, 785, 65
Calzetti, D., Armus, L., Bohlin, R. C., et al. 2000, ApJ, 533, 682
Carnall, A. C., McLure, R. J., Dunlop, J. S., & Davé, R. 2018, MNRAS, 480, 4379
Carniani, S., Hainline, K., D'Eugenio, F., et al. 2024, Nature, 633, 318
Casey, C. M., Kartaltepe, J. S., Drakos, N. E., et al. 2023, ApJ, 954, 31
Castellano, M., Fontana, A., Treu, T., et al. 2022, ApJ, 938, L15
Castellano, M., Napolitano, L., Fontana, A., et al. 2024, ApJ, 972, 143
Chabrier, G. 2003, PASP, 115, 763
Chemerynska, I., Atek, H., Furtak, L. J., et al. 2024, MNRAS, 531, 2615
Claeyssens, A., Richard, J., Blaizot, J., et al. 2022, A&A, 666, A78
Cuillandre, J.-C., Bertin, E., Bolzonella, M., et al. 2025, A&A, 697, A6
Dayal, P., Ferrara, A., Dunlop, J. S., & Pacucci, F. 2014, MNRAS, 445, 2545
Dayal, P., Ferrara, A., Sommovigo, L., et al. 2022, MNRAS, 512, 989
Donnan, C. T., Dunlop, J. S., McLure, R. J., McLeod, D. J., & Cullen, F. 2025, MNRAS, 539, 2409
Donnan, C. T., McLeod, D. J., Dunlop, J. S., et al. 2023, MNRAS, 518, 6011
Donnan, C. T., McLure, R. J., Dunlop, J. S., et al. 2024, MNRAS, 533, 3222
Drakos, N. E., Villasenor, B., Robertson, B. E., et al. 2022, ApJ, 926, 194
Duncan, K. J., McLeod, D. J., Best, P. N., et al. 2025, MNRAS, 541, 1329
Dunlop, J. S., Bowler, R. A. A., Franx, M., et al. 2023, in A Decade of ESO Wide-field Imaging Surveys, ESO (Garching, Germany: Zenodo)
Endsley, R., Stark, D. P., Charlot, S., et al. 2021a, MNRAS, 502, 6044
Endsley, R., Stark, D. P., Chevallard, J., & Charlot, S. 2021b, MNRAS, 500, 5229
Euclid Collaboration: Barnett, R., Warren, S. J., Mortlock, D. J., et al. 2019, A&A, 631, A85
Euclid Collaboration: Cropper, M., Al-Bahlawan, A., Amiaux, J., et al. 2025, A&A, 697, A2
Euclid Collaboration: Jahnke, K., Gillard, W., Schirmer, M., et al. 2025, A&A, 697, A3
Euclid Collaboration: McPartland, C. J. R., Zalesky, L., Weaver, J. R., et al. 2025, A&A, 695, A259
Euclid Collaboration: Mellier, Y., Abdurro'uf, Acevedo Barroso, J., et al. 2025, A&A, 697, A1
Euclid Collaboration: Moneti, A., McCracken, H. J., Shuntov, M., et al. 2022, A&A, 658, A126
Euclid Collaboration: Scaramella, R., Amiaux, J., Mellier, Y., et al. 2022, A&A, 662, A112
Euclid Collaboration: van Mierlo, S. E., Caputi, K. I., Ashby, M., et al. 2022, A&A, 666, A200
Ferrara, A., Pallottini, A., & Dayal, P. 2023, MNRAS, 522, 3986
Finkelstein, S. L. & Bagley, M. B. 2022, ApJ, 938, 25
Finkelstein, S. L., Bagley, M. B., Arrabal Haro, P., et al. 2022, ApJ, 940, L55
Finkelstein, S. L., Ryan, Jr., R. E., Papovich, C., et al. 2015, ApJ, 810, 71
Franco, M., Casey, C. M., Akins, H. B., et al. 2025, arXiv e-prints, arXiv:2508.04791
Gaia Collaboration, Brown, A. G. A., Vallenari, A., et al. 2021, A&A, 649, A1
Gaia Collaboration, Vallenari, A., Brown, A. G. A., et al. 2023, A&A, 674, A1
Gehrels, N. 1986, ApJ, 303, 336
Grazian, A., Castellano, M., Fontana, A., et al. 2012, A&A, 547, A51
Greene, J. E., Labbe, I., Goulding, A. D., et al. 2024, ApJ, 964, 39
Guhathakurta, P., Tyson, J. A., & Majewski, S. R. 1990, ApJ, 357, L9
Harikane, Y., Inoue, A. K., Ellis, R. S., et al. 2025, ApJ, 980, 138
Harikane, Y., Ono, Y., Ouchi, M., et al. 2022, ApJS, 259, 20
Harikane, Y., Ouchi, M., Oguri, M., et al. 2023a, ApJS, 265, 5
Harikane, Y., Zhang, Y., Nakajima, K., et al. 2023b, ApJ, 959, 39
Hu, W., Wang, J., Zheng, Z.-Y., et al. 2017, ApJ, 845, L16
Ilbert, O., Arnouts, S., McCracken, H. J., et al. 2006, A&A, 457, 841
Inami, H., Algera, H. S. B., Schouws, S., et al. 2022, MNRAS, 515, 3126
Jarvis, M. J., Bonfield, D. G., Bruce, V. A., et al. 2013, MNRAS, 428, 1281
Kannan, R., Garaldi, E., Smith, A., et al. 2022, MNRAS, 511, 4005
Kartaltepe, J. S., Rose, C., Vanderhoof, B. N., et al. 2023, ApJ, 946, L15
Kauffmann, O. B., Ilbert, O., Weaver, J. R., et al. 2022, A&A, 667, A65
Kiyota, T., Ouchi, M., Xu, Y., et al. 2025, ApJ, 995, 150
Kocevski, D. D., Finkelstein, S. L., Barro, G., et al. 2025, ApJ, 986, 126
Kron, R. G. 1980, ApJS, 43, 305
Labbé, I., van Dokkum, P., Nelson, E., et al. 2023, Nature, 616, 266
Laigle, C., McCracken, H. J., Ilbert, O., et al. 2016, ApJS, 224, 24
Lambert, T. S., Assef, R. J., Mazzucchelli, C., et al. 2024, A&A, 689, A331
Lawrence, A., Warren, S. J., Almaini, O., et al. 2007, MNRAS, 379, 1599
Le Bail, A., Daddi, E., Elbaz, D., et al. 2024, A&A, 688, A53
Lines, N. E. P., Bowler, R. A. A., Adams, N. J., et al. 2025, MNRAS, 539, 2685
Liu, C., Mutch, S. J., Angel, P. W., et al. 2016, MNRAS, 462, 235
Lovell, C. C., Vijayan, A. P., Thomas, P. A., et al. 2021, MNRAS, 500, 2127
Luhman, K. L., Alves de Oliveira, C., Baraffe, I., et al. 2024, ApJ, 975, 162
Madau, P. 1995, ApJ, 441, 18
Marconcini, C., D'Eugenio, F., Maiolino, R., et al. 2025, A&A, 699, A154
Mason, C. A., Treu, T., Schmidt, K. B., et al. 2015, ApJ, 805, 79
Matthee, J., Naidu, R. P., Brammer, G., et al. 2024, ApJ, 963, 129
McCracken, H. J., Milvang-Jensen, B., Dunlop, J., et al. 2012, A&A, 544, A156
McLeod, D. J., Donnan, C. T., McLure, R. J., et al. 2024, MNRAS, 527, 5004
McLeod, D. J., McLure, R. J., & Dunlop, J. S. 2016, MNRAS, 459, 3812
McLure, R. J., Cirasuolo, M., Dunlop, J. S., Foucaud, S., & Almaini, O. 2009, MNRAS, 395, 2196
McLure, R. J., Dunlop, J. S., Bowler, R. A. A., et al. 2013, MNRAS, 432, 2696
Morishita, T., Stiavelli, M., Chary, R.-R., et al. 2024, ApJ, 963, 9
Naidu, R. P., Oesch, P. A., van Dokkum, P., et al. 2022, ApJ, 940, L14
Nikopoulos, G. P. & Dayal, P. 2024, arXiv:2409.10613
Ocvirk, P., Gillet, N., Shapiro, P. R., et al. 2016, MNRAS, 463, 1462
Oesch, P. A., Bouwens, R. J., Carollo, C. M., et al. 2010, ApJ, 709, L21
Oesch, P. A., van Dokkum, P. G., Illingworth, G. D., et al. 2015, ApJ, 804, L30
Oke, J. B. & Gunn, J. E. 1983, ApJ, 266, 713
Ono, Y., Ouchi, M., Harikane, Y., et al. 2018, PASJ, 70, S10
Ormerod, K., Conselice, C. J., Adams, N. J., et al. 2024, MNRAS, 527, 6110
Ouchi, M., Ellis, R., Ono, Y., et al. 2013, ApJ, 778, 102
Peng, Y.-j., Lilly, S. J., Kovač, K., et al. 2010, ApJ, 721, 193
Pirie, C. A., Best, P. N., Duncan, K. J., et al. 2025, MNRAS, 541, 1348
Roberts-Borsani, G. W., Bouwens, R. J., Oesch, P. A., et al. 2016, ApJ, 823, 143
Rodighiero, G., Vaccari, M., Franceschini, A., et al. 2010, A&A, 515, A8
Rojas-Ruiz, S., Bagley, M., Roberts-Borsani, G., et al. 2025, ApJ, 985, 80
Roper, W. J., Lovell, C. C., Vijayan, A. P., et al. 2022, MNRAS, 514, 1921
Ryan, R. E., Thorman, P. A., Yan, H., et al. 2011, ApJ, 739, 83
Sanders, D. B., Salvato, M., Aussel, H., et al. 2007, ApJS, 172, 86
Schenker, M. A., Stark, D. P., Ellis, R. S., et al. 2012, ApJ, 744, 179
Schmidt, M. 1968, ApJ, 151, 393
Scoville, N., Aussel, H., Brusa, M., et al. 2007, ApJS, 172, 1
Shibuya, T., Ouchi, M., & Harikane, Y. 2015, ApJS, 219, 15
Shuntov, Marko, Akins, Hollis B., Paquereau, Louise, et al. 2025, A&A, 704, A339
Smit, R., Bouwens, R. J., Franx, M., et al. 2015, ApJ, 801, 122
Sobral, D., Matthee, J., Darvish, B., et al. 2015, ApJ, 808, 139
Stanway, E. R., Bremer, M. N., Squitieri, V., Douglas, L. S., & Lehnert, M. D. 2008, MNRAS, 386, 370
Stark, D. P. 2016, ARA&A, 54, 761
Stark, D. P., Schenker, M. A., Ellis, R., et al. 2013, ApJ, 763, 129
Stefanon, M., Labbé, I., Bouwens, R. J., et al. 2017, ApJ, 851, 43
Stefanon, M., Labbé, I., Bouwens, R. J., et al. 2019, ApJ, 883, 99

Steidel, C. C., Giavalisco, M., Pettini, M., Dickinson, M., & Adelberger, K. L. 1996, ApJ, 462, L17
Trenti, M. & Stiavelli, M. 2008, ApJ, 676, 767
Umeda, H., Ouchi, M., Kikuta, S., et al. 2025, ApJS, 277, 37
Varadaraj, R. G., Bowler, R. A. A., Jarvis, M. J., Adams, N. J., & Häußler, B. 2023, MNRAS, 524, 4586
Vijayan, A. P., Lovell, C. C., Wilkins, S. M., et al. 2021, MNRAS, 501, 3289
Weaver, J., Taamoli, S., McPartland, C., et al. 2025, A&A, 697, A16
Weaver, J. R., Kauffmann, O. B., Ilbert, O., et al. 2022, ApJS, 258, 11
Westcott, L., Conselice, C. J., Harvey, T., et al. 2025, ApJ, 983, 121
Whitler, L., Stark, D. P., Endsley, R., et al. 2023, MNRAS, 519, 5859
Whitler, L., Stark, D. P., Topping, M. W., et al. 2025, ApJ, 992, 63
Wilkins, S. M., Stanway, E. R., & Bremer, M. N. 2014, MNRAS, 439, 1038
Wilkins, S. M., Vijayan, A. P., Lovell, C. C., et al. 2023, MNRAS, 519, 3118
Yang, L., Leethochawalit, N., Treu, T., et al. 2022, MNRAS, 514, 1148
Yung, L. Y. A., Somerville, R. S., Finkelstein, S. L., Popping, G., & Davé, R. 2019, MNRAS, 483, 2983

[1] Department of Physics, Oxford University, Keble Road, Oxford OX1 3RH, UK
[2] Jodrell Bank Centre for Astrophysics, Department of Physics and Astronomy, University of Manchester, Oxford Road, Manchester M13 9PL, UK
[3] Department of Physics and Astronomy, University of the Western Cape, Bellville, Cape Town, 7535, South Africa
[4] MIT Kavli Institute for Astrophysics and Space Research, Massachusetts Institute of Technology, Cambridge, MA 02139, USA
[5] Max-Planck-Institut für Astronomie, Königstuhl 17, 69117 Heidelberg, Germany
[6] Institute of Cosmology and Gravitation, University of Portsmouth, Portsmouth PO1 3FX, UK
[7] Kapteyn Astronomical Institute, University of Groningen, PO Box 800, 9700 AV Groningen, The Netherlands
[8] Cosmic Dawn Center (DAWN)
[9] Department of Physics & Astronomy, University of Sussex, Brighton BN1 9QH, UK
[10] Leiden Observatory, Leiden University, Einsteinweg 55, 2333 CC Leiden, The Netherlands
[11] Niels Bohr Institute, University of Copenhagen, Jagtvej 128, 2200 Copenhagen, Denmark
[12] Department of Astronomy, University of Geneva, ch. d'Ecogia 16, 1290 Versoix, Switzerland
[13] School of Mathematics and Physics, University of Surrey, Guildford, Surrey, GU2 7XH, UK
[14] INAF-Osservatorio Astronomico di Brera, Via Brera 28, 20122 Milano, Italy
[15] INAF-Osservatorio di Astrofisica e Scienza dello Spazio di Bologna, Via Piero Gobetti 93/3, 40129 Bologna, Italy
[16] IFPU, Institute for Fundamental Physics of the Universe, via Beirut 2, 34151 Trieste, Italy
[17] INAF-Osservatorio Astronomico di Trieste, Via G. B. Tiepolo 11, 34143 Trieste, Italy
[18] INFN, Sezione di Trieste, Via Valerio 2, 34127 Trieste TS, Italy
[19] SISSA, International School for Advanced Studies, Via Bonomea 265, 34136 Trieste TS, Italy
[20] Dipartimento di Fisica e Astronomia, Università di Bologna, Via Gobetti 93/2, 40129 Bologna, Italy
[21] INFN-Sezione di Bologna, Viale Berti Pichat 6/2, 40127 Bologna, Italy
[22] Dipartimento di Fisica, Università di Genova, Via Dodecaneso 33, 16146, Genova, Italy
[23] INFN-Sezione di Genova, Via Dodecaneso 33, 16146, Genova, Italy
[24] Department of Physics "E. Pancini", University Federico II, Via Cinthia 6, 80126, Napoli, Italy
[25] INAF-Osservatorio Astronomico di Capodimonte, Via Moiariello 16, 80131 Napoli, Italy
[26] Dipartimento di Fisica, Università degli Studi di Torino, Via P. Giuria 1, 10125 Torino, Italy
[27] INFN-Sezione di Torino, Via P. Giuria 1, 10125 Torino, Italy
[28] INAF-Osservatorio Astrofisico di Torino, Via Osservatorio 20, 10025 Pino Torinese (TO), Italy
[29] European Space Agency/ESTEC, Keplerlaan 1, 2201 AZ Noordwijk, The Netherlands
[30] INAF-IASF Milano, Via Alfonso Corti 12, 20133 Milano, Italy
[31] Centro de Investigaciones Energéticas, Medioambientales y Tecnológicas (CIEMAT), Avenida Complutense 40, 28040 Madrid, Spain
[32] Port d'Informació Científica, Campus UAB, C. Albareda s/n, 08193 Bellaterra (Barcelona), Spain
[33] INAF-Osservatorio Astronomico di Roma, Via Frascati 33, 00078 Monteporzio Catone, Italy
[34] INFN section of Naples, Via Cinthia 6, 80126, Napoli, Italy
[35] Institute for Astronomy, University of Hawaii, 2680 Woodlawn Drive, Honolulu, HI 96822, USA
[36] Dipartimento di Fisica e Astronomia "Augusto Righi" - Alma Mater Studiorum Università di Bologna, Viale Berti Pichat 6/2, 40127 Bologna, Italy
[37] Instituto de Astrofísica de Canarias, Vía Láctea, 38205 La Laguna, Tenerife, Spain
[38] Institute for Astronomy, University of Edinburgh, Royal Observatory, Blackford Hill, Edinburgh EH9 3HJ, UK
[39] European Space Agency/ESRIN, Largo Galileo Galilei 1, 00044 Frascati, Roma, Italy
[40] ESAC/ESA, Camino Bajo del Castillo, s/n., Urb. Villafranca del Castillo, 28692 Villanueva de la Cañada, Madrid, Spain
[41] Université Claude Bernard Lyon 1, CNRS/IN2P3, IP2I Lyon, UMR 5822, Villeurbanne, F-69100, France
[42] Institut de Ciències del Cosmos (ICCUB), Universitat de Barcelona (IEEC-UB), Martí i Franquès 1, 08028 Barcelona, Spain
[43] Institució Catalana de Recerca i Estudis Avançats (ICREA), Passeig de Lluís Companys 23, 08010 Barcelona, Spain
[44] Institut de Ciencies de l'Espai (IEEC-CSIC), Campus UAB, Carrer de Can Magrans, s/n Cerdanyola del Vallés, 08193 Barcelona, Spain
[45] UCB Lyon 1, CNRS/IN2P3, IUF, IP2I Lyon, 4 rue Enrico Fermi, 69622 Villeurbanne, France
[46] Mullard Space Science Laboratory, University College London, Holmbury St Mary, Dorking, Surrey RH5 6NT, UK
[47] Departamento de Física, Faculdade de Ciências, Universidade de Lisboa, Edifício C8, Campo Grande, PT1749-016 Lisboa, Portugal
[48] Instituto de Astrofísica e Ciências do Espaço, Faculdade de Ciências, Universidade de Lisboa, Campo Grande, 1749-016 Lisboa, Portugal
[49] Université Paris-Saclay, CNRS, Institut d'astrophysique spatiale, 91405, Orsay, France
[50] INFN-Padova, Via Marzolo 8, 35131 Padova, Italy
[51] Aix-Marseille Université, CNRS/IN2P3, CPPM, Marseille, France
[52] INAF-Istituto di Astrofisica e Planetologia Spaziali, via del Fosso del Cavaliere, 100, 00100 Roma, Italy
[53] Space Science Data Center, Italian Space Agency, via del Politecnico snc, 00133 Roma, Italy
[54] INFN-Bologna, Via Irnerio 46, 40126 Bologna, Italy
[55] Institut d'Estudis Espacials de Catalunya (IEEC), Edifici RDIT, Campus UPC, 08860 Castelldefels, Barcelona, Spain
[56] Institute of Space Sciences (ICE, CSIC), Campus UAB, Carrer de Can Magrans, s/n, 08193 Barcelona, Spain
[57] University Observatory, LMU Faculty of Physics, Scheinerstrasse 1, 81679 Munich, Germany
[58] Max Planck Institute for Extraterrestrial Physics, Giessenbachstr. 1, 85748 Garching, Germany
[59] INAF-Osservatorio Astronomico di Padova, Via dell'Osservatorio 5, 35122 Padova, Italy
[60] Universitäts-Sternwarte München, Fakultät für Physik, Ludwig-Maximilians-Universität München, Scheinerstrasse 1, 81679 München, Germany
[61] Dipartimento di Fisica "Aldo Pontremoli", Università degli Studi di Milano, Via Celoria 16, 20133 Milano, Italy
[62] INFN-Sezione di Milano, Via Celoria 16, 20133 Milano, Italy

[63] Institute of Theoretical Astrophysics, University of Oslo, P.O. Box 1029 Blindern, 0315 Oslo, Norway
[64] Jet Propulsion Laboratory, California Institute of Technology, 4800 Oak Grove Drive, Pasadena, CA, 91109, USA
[65] Department of Physics, Lancaster University, Lancaster, LA1 4YB, UK
[66] Felix Hormuth Engineering, Goethestr. 17, 69181 Leimen, Germany
[67] Technical University of Denmark, Elektrovej 327, 2800 Kgs. Lyngby, Denmark
[68] Cosmic Dawn Center (DAWN), Denmark
[69] NASA Goddard Space Flight Center, Greenbelt, MD 20771, USA
[70] Department of Physics and Astronomy, University College London, Gower Street, London WC1E 6BT, UK
[71] Department of Physics and Helsinki Institute of Physics, Gustaf Hällströmin katu 2, University of Helsinki, 00014 Helsinki, Finland
[72] Université Paris-Saclay, Université Paris Cité, CEA, CNRS, AIM, 91191, Gif-sur-Yvette, France
[73] Université de Genève, Département de Physique Théorique and Centre for Astroparticle Physics, 24 quai Ernest-Ansermet, CH-1211 Genève 4, Switzerland
[74] Department of Physics, P.O. Box 64, University of Helsinki, 00014 Helsinki, Finland
[75] Helsinki Institute of Physics, Gustaf Hällströmin katu 2, University of Helsinki, 00014 Helsinki, Finland
[76] Laboratoire d'etude de l'Univers et des phenomenes eXtremes, Observatoire de Paris, Université PSL, Sorbonne Université, CNRS, 92190 Meudon, France
[77] SKAO, Jodrell Bank, Lower Withington, Macclesfield SK11 9FT, United Kingdom
[78] Centre de Calcul de l'IN2P3/CNRS, 21 avenue Pierre de Coubertin 69627 Villeurbanne Cedex, France
[79] Universität Bonn, Argelander-Institut für Astronomie, Auf dem Hügel 71, 53121 Bonn, Germany
[80] INFN-Sezione di Roma, Piazzale Aldo Moro, 2 - c/o Dipartimento di Fisica, Edificio G. Marconi, 00185 Roma, Italy
[81] Aix-Marseille Université, CNRS, CNES, LAM, Marseille, France
[82] Dipartimento di Fisica e Astronomia "Augusto Righi" - Alma Mater Studiorum Università di Bologna, via Piero Gobetti 93/2, 40129 Bologna, Italy
[83] Department of Physics, Institute for Computational Cosmology, Durham University, South Road, Durham, DH1 3LE, UK
[84] Université Paris Cité, CNRS, Astroparticule et Cosmologie, 75013 Paris, France
[85] CNRS-UCB International Research Laboratory, Centre Pierre Binétruy, IRL2007, CPB-IN2P3, Berkeley, USA
[86] University of Applied Sciences and Arts of Northwestern Switzerland, School of Engineering, 5210 Windisch, Switzerland
[87] Institut d'Astrophysique de Paris, 98bis Boulevard Arago, 75014, Paris, France
[88] Institut d'Astrophysique de Paris, UMR 7095, CNRS, and Sorbonne Université, 98 bis boulevard Arago, 75014 Paris, France
[89] Institute of Physics, Laboratory of Astrophysics, Ecole Polytechnique Fédérale de Lausanne (EPFL), Observatoire de Sauverny, 1290 Versoix, Switzerland
[90] Telespazio UK S.L. for European Space Agency (ESA), Camino bajo del Castillo, s/n, Urbanizacion Villafranca del Castillo, Villanueva de la Cañada, 28692 Madrid, Spain
[91] Institut de Física d'Altes Energies (IFAE), The Barcelona Institute of Science and Technology, Campus UAB, 08193 Bellaterra (Barcelona), Spain
[92] DARK, Niels Bohr Institute, University of Copenhagen, Jagtvej 155, 2200 Copenhagen, Denmark
[93] Waterloo Centre for Astrophysics, University of Waterloo, Waterloo, Ontario N2L 3G1, Canada
[94] Department of Physics and Astronomy, University of Waterloo, Waterloo, Ontario N2L 3G1, Canada
[95] Perimeter Institute for Theoretical Physics, Waterloo, Ontario N2L 2Y5, Canada
[96] Centre National d'Etudes Spatiales – Centre spatial de Toulouse, 18 avenue Edouard Belin, 31401 Toulouse Cedex 9, France
[97] Institute of Space Science, Str. Atomistilor, nr. 409 Măgurele, Ilfov, 077125, Romania
[98] Dipartimento di Fisica e Astronomia "G. Galilei", Università di Padova, Via Marzolo 8, 35131 Padova, Italy
[99] Institut für Theoretische Physik, University of Heidelberg, Philosophenweg 16, 69120 Heidelberg, Germany
[100] Institut de Recherche en Astrophysique et Planétologie (IRAP), Université de Toulouse, CNRS, UPS, CNES, 14 Av. Edouard Belin, 31400 Toulouse, France
[101] Université St Joseph; Faculty of Sciences, Beirut, Lebanon
[102] Departamento de Física, FCFM, Universidad de Chile, Blanco Encalada 2008, Santiago, Chile
[103] Universität Innsbruck, Institut für Astro- und Teilchenphysik, Technikerstr. 25/8, 6020 Innsbruck, Austria
[104] Satlantis, University Science Park, Sede Bld 48940, Leioa-Bilbao, Spain
[105] Infrared Processing and Analysis Center, California Institute of Technology, Pasadena, CA 91125, USA
[106] Instituto de Astrofísica e Ciências do Espaço, Faculdade de Ciências, Universidade de Lisboa, Tapada da Ajuda, 1349-018 Lisboa, Portugal
[107] Universidad Politécnica de Cartagena, Departamento de Electrónica y Tecnología de Computadoras, Plaza del Hospital 1, 30202 Cartagena, Spain
[108] Aurora Technology for European Space Agency (ESA), Camino bajo del Castillo, s/n, Urbanizacion Villafranca del Castillo, Villanueva de la Cañada, 28692 Madrid, Spain
[109] ICL, Junia, Université Catholique de Lille, LITL, 59000 Lille, France
[110] ICSC - Centro Nazionale di Ricerca in High Performance Computing, Big Data e Quantum Computing, Via Magnanelli 2, Bologna, Italy

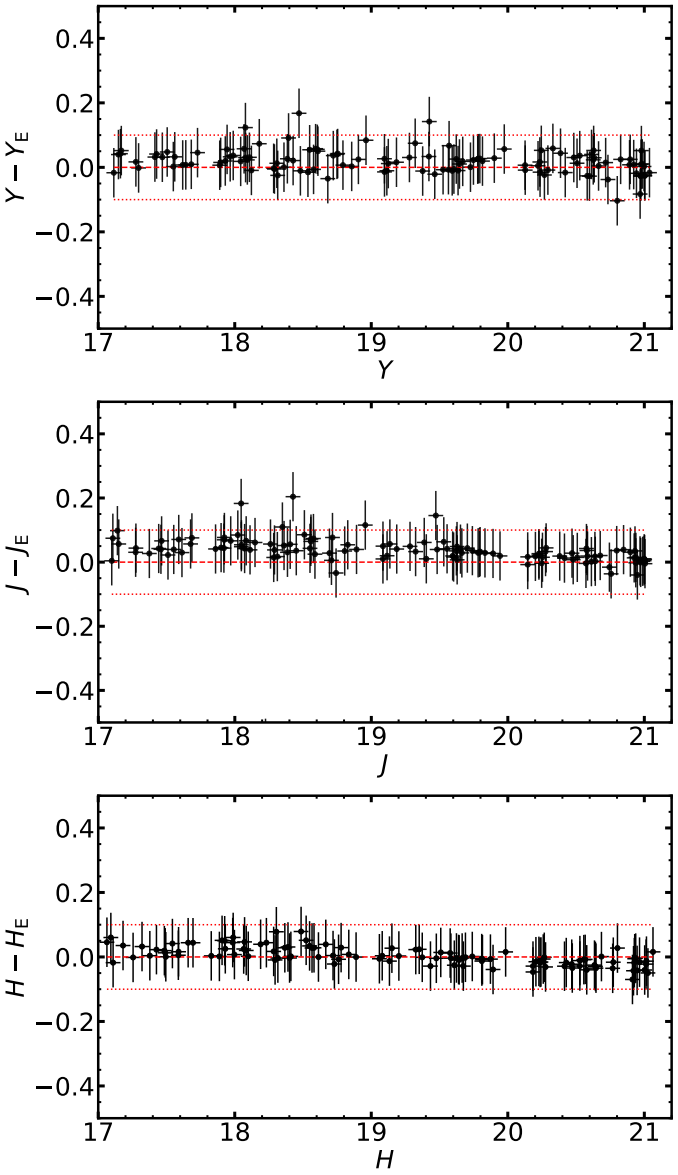

Fig. A.1: The difference in magnitude between VISTA Y and *Euclid* Y_E (*top*), VISTA J and *Euclid* J_E (*middle*), and VISTA H and *Euclid* H_E (*bottom*) and for bright stars with flat colours in VISTA, selected as $|Y - J| < 0.05 \wedge |J - H| < 0.05$. The red dashed line indicates no colour difference, and the red dotted lines indicate a difference in magnitude of 0.1. A minimum uncertainty of 5% is imposed on the photometry.

Appendix A: *Euclid* photometry check

In Fig. A.1 we present the colours in comparable *Euclid* and VISTA filters of stars with flat YJH photometry. This provides a check that the *Euclid* photometry, after PSF homogenisation, is consistent with VISTA.

Appendix B: Comparison of M_{UV} and z_{phot} between the U-only and U+E samples

In Fig. B.1 we show the differences in the determination of the absolute rest-frame UV magnitude M_{UV} with and without *Euclid* photometry, along with a similar plot for the photometric redshifts z_{phot}.

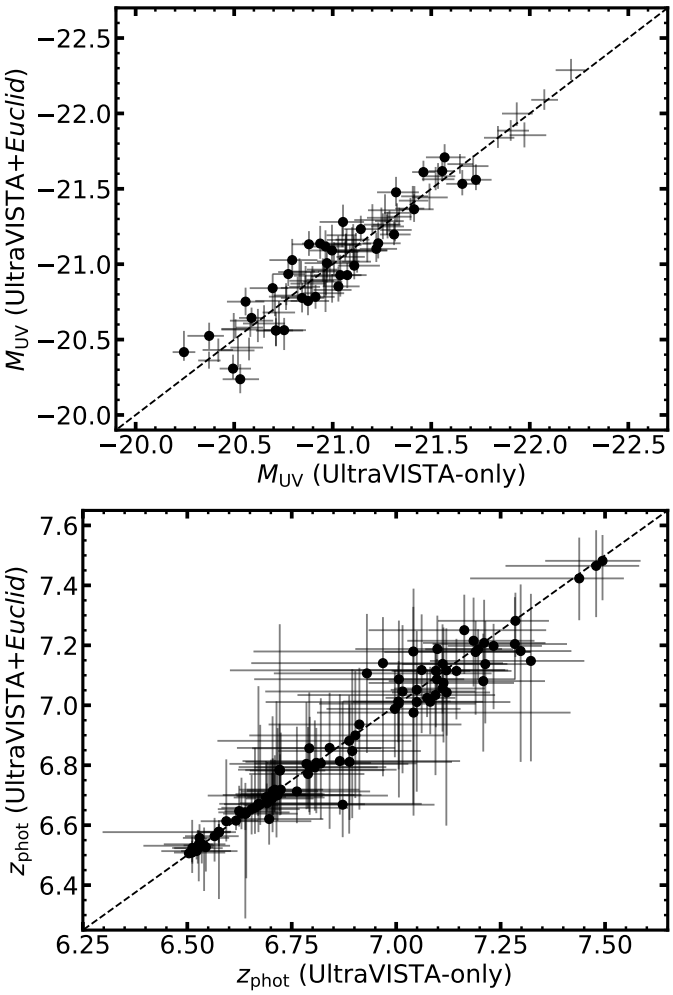

Fig. B.1: A comparison between the M_{UV} (*top*) and z_{phot} (*bottom*) derived with and without *Euclid* photometry. The sample here is based on sources which are present in both the U-only and U+E samples. In the top panel, the large black points indicate sources which have their M_{UV} change enough after the inclusion of *Euclid* photometry that they move into a different LF M_{UV} bin. In both panels the dashed line shows the one-to-one relation.

Appendix C: SED fits and postage stamp images

In Fig. C.1 we present the results of the SED fitting and postage stamp images for the 30 most luminous galaxies in the U+E sample, spanning $-22.3 < M_{UV} < -21.3$.

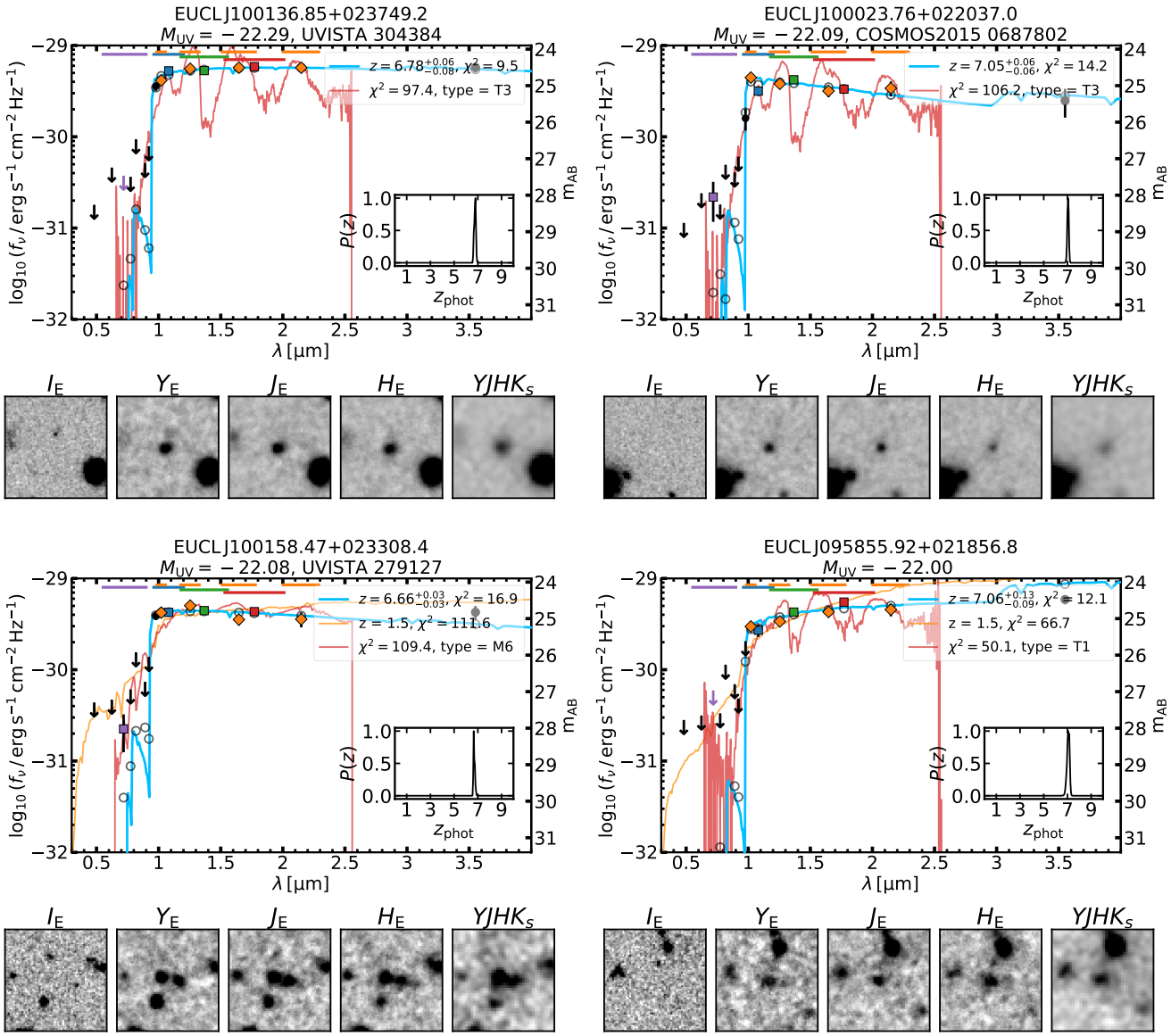

Fig. C.1: SED fits (*top*) and postage stamp cutouts (*bottom*) of the thirty most luminous galaxies in the U+E sample. See Fig. 3 for a description of the SED plots. The title of the SED indicates the object ID, absolute magnitude M_{UV}, and the literature ID if it has been previously identified. The postage stamps, from left to right, are from I_E, Y_E, J_E, H_E, and a VISTA $YJHK_s$ stack. The stamps are $6'' \times 6''$ and are scaled to saturate at 5σ above and 2σ below the noise level. Objects with names beginning with UVISTA were identified in Bowler et al. (2014). Objects with names labelled as [ESC2021] and [ESC2021a] were first identified in Endsley et al. (2021b) and Endsley et al. (2021a), respectively. [DMD23] 892014 is from Donnan et al. (2023). COSMOS2015 and COSMOS2020 objects were identified in Laigle et al. (2016) and Weaver et al. (2022), respectively. S-CANDELS objects are galaxies identified in HST imaging (Ashby et al. 2015), and LAE-17 was identified in Hu et al. (2017). The SSTSL source is also identified as REBELS-21 (Bouwens et al. 2022).

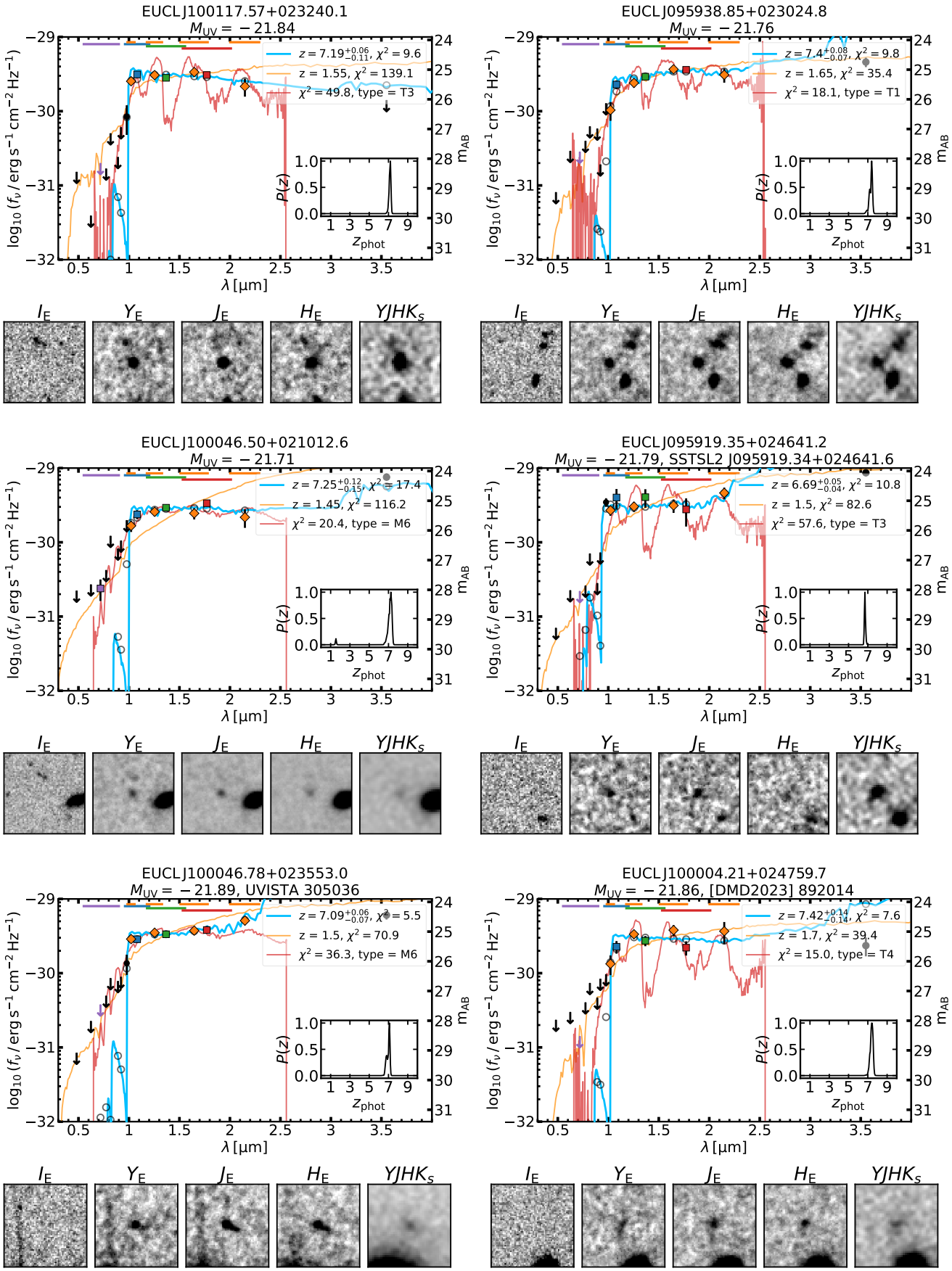

Fig. C.1: Continued.

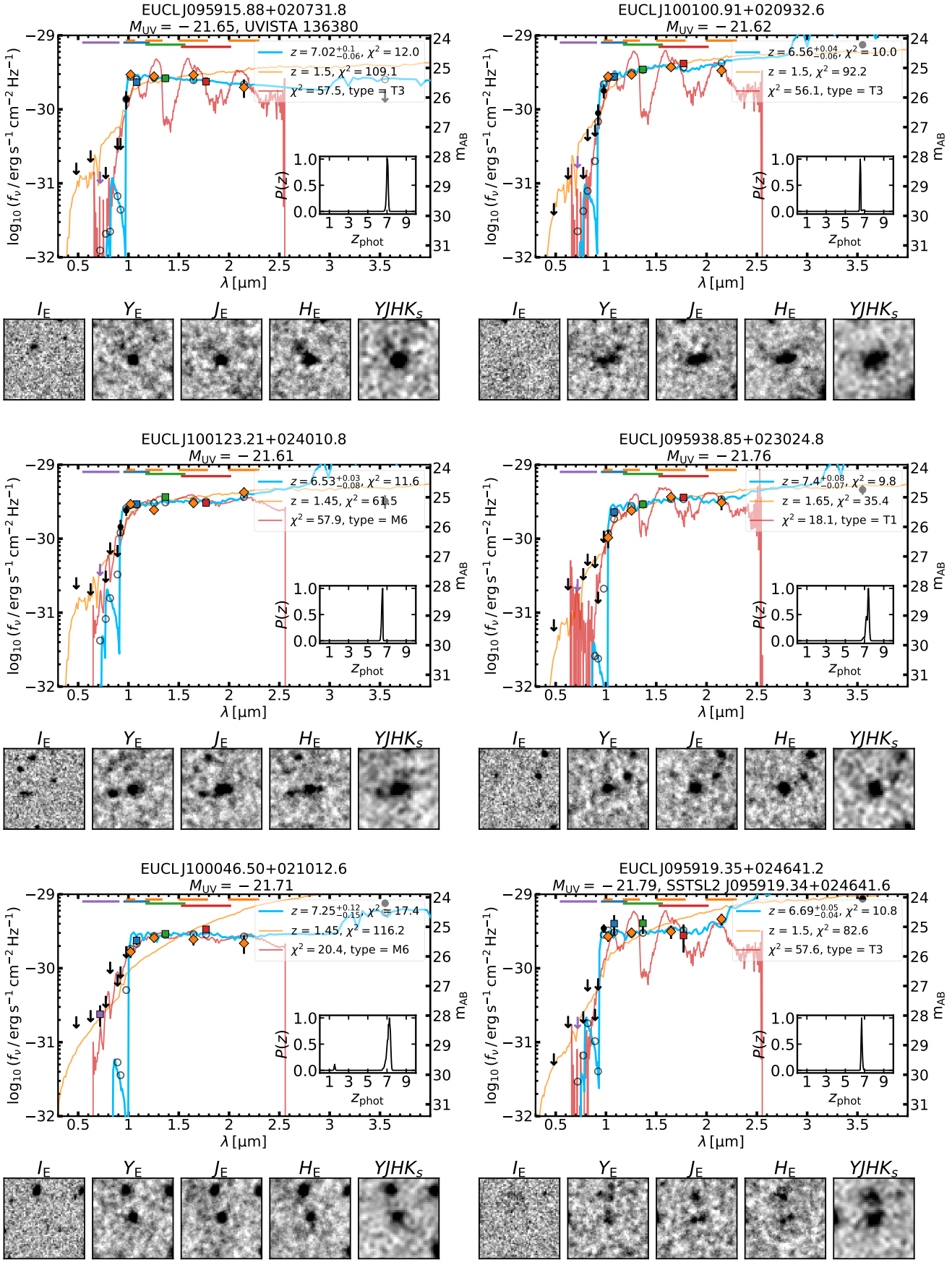

Fig. C.1: Continued.

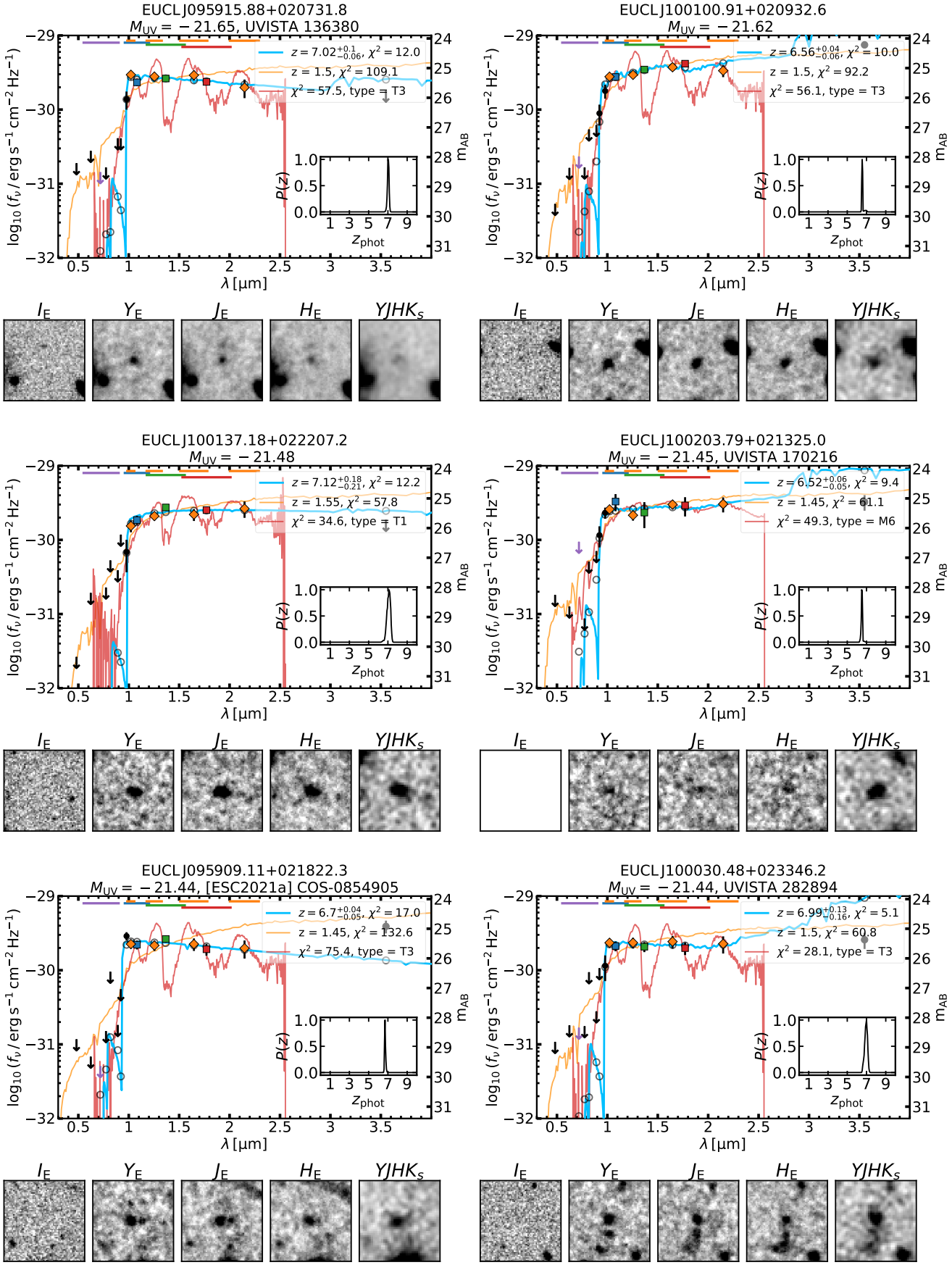

Fig. C.1: Continued.

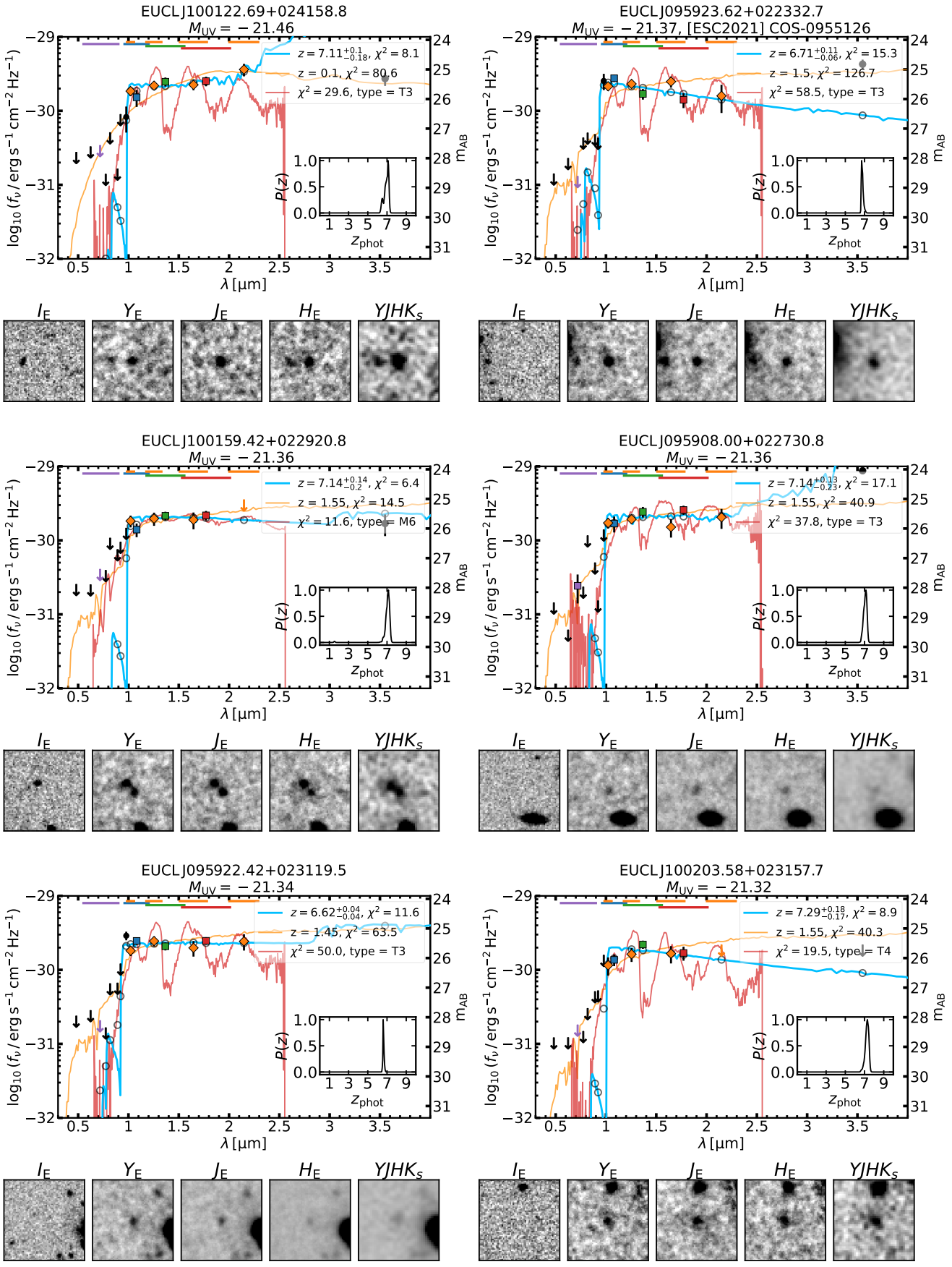

Fig. C.1: Continued.

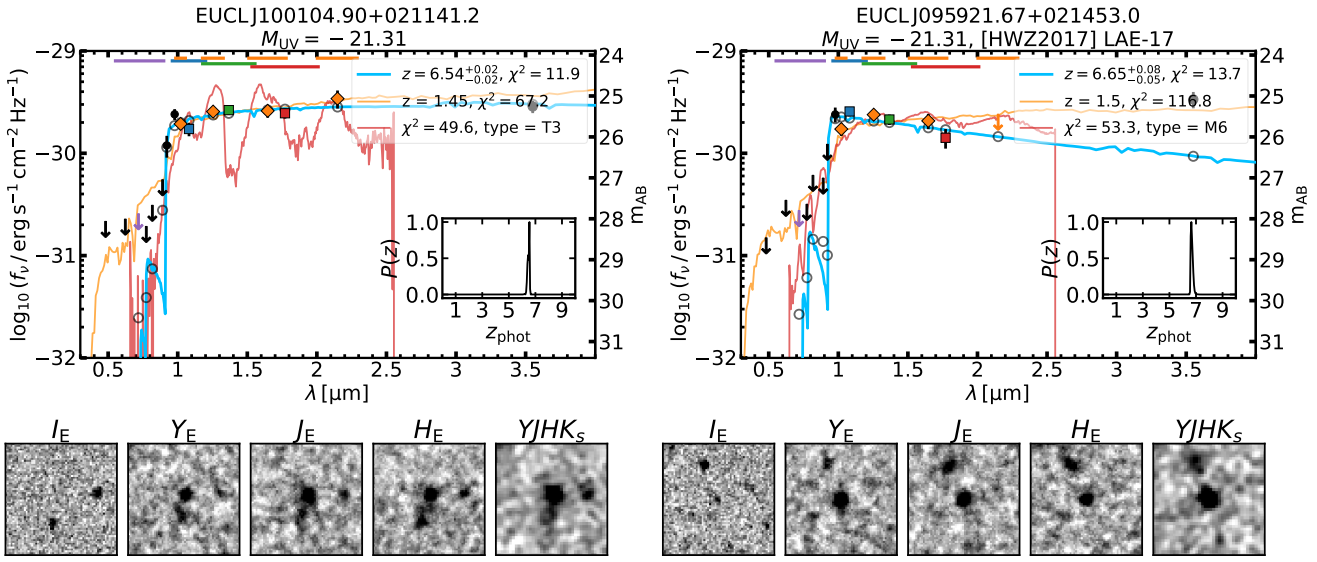

Fig. C.1: Continued.